3D Printed Highly Integrated Microwave Components for Arrays and Sensing

by

Mohammadreza Ranjbar Naeini

A dissertation submitted in partial fulfillment of
the requirements for the degree of

Doctor of Philosophy

(Electrical Engineering)

at the

UNIVERSITY OF WISCONSIN–MADISON

2021

Date of final oral examination: 06/24/2021
The dissertation is approved by the following members of the Final Oral Committee:
Daniel van der Weide, Professor, Electrical and Computer Engineering
John H. Booske, Professor, Electrical and Computer Engineering
Zongfu Yu, Associate Professor, Electrical and Computer Engineering
Peter Timbie, Professor, Physics

Acknowledgements

I wish to express my heartfelt appreciation to the following individuals, whose advice and support I am deeply thankful for.

Foremost, I would like to thank my advisor and mentor, Professor Daniel van der Weide. I learned a new way of thinking when facing challenges. We always came up with novel ideas in our discussions which were guiding me in my progress. With having the freedom to try those ideas during the past years of my study, I could grow as a researcher. Also, I am deeply grateful for his encouragements and support.

I would also like to thank the members of my doctoral committee for their time and valuable suggestions: Professors John Booske, Zongfu Yu, and Peter Timbie.

I would like to thank my vdW group members for offering their knowledge and aid in assisting me in my research: Marcos Martinez, Matt Dwyer, Yuchen Gu. They have made this experience much more pleasant with their warm presence and friendship. I highly appreciate Yuchen's help in building the near-field measurement setup.

I extend my sincere gratitude to my first and best teachers, my parents, Ahmad and Mitra, for their everlasting love, dedication, and encouragement.

Abstract

Every decade new technologies revolutionize industries and academic research. 3D-printing is one of them that not only has taken the place of some conventional fabrication methods but also has brought in new applications to many fields. Communication is one of the fields that can take advantage of this new area as it includes antenna prototyping and large-scale fabrication of them. Mostly, antenna design is based on PCB fabrication as it is widely accessible, quick, and low-cost. But such antenna design is limited to planar structures while tolerating dielectric loss of the substrates. 3D-printing enables designing novel 3D antennas with almost any interior features with quick, accurate, and low-cost fabrication. This can change antenna design in long term and introduce new concepts and applications in the field of communications. Recently, this field of research has received more interests as some 3D-printing materials have been developed with very low-loss and variety of dielectric constants for communication purposes, moving forward this technology in antenna design.

In this research, first, 3D-printing of microwave components and antennas in plastic and then copper coating them via airbrushing was evaluated. Then, based on the acceptable performance, novel antennas designed based on accommodations that 3D-printing gives us. For instance, water soluble 3D-

printing materials, such as PVA, can support the main body while printing and can be removed with no need to getting access to inside of the structure. This lets us think of new designs with fine interior features while keeping the fabrication monolithic. Therefore, 3D-printing can change the usual antenna design which was based on PCB. On the other hand, based on the nature of 3D-prining, some 3D structures, which were hard to fabricate, can be realized. For example, in this research, two novel antennas are designed based on being able to print 3D structures easily, quick and with low-cost.

The purpose of new technologies is to ease the life. But they can introduce new challenges for the engineers to overcome. For instance, the second frequency spectrum of 5G, FR2, is set to a bandwidth with the center frequency of above 24 GHz. It means cellular phones, 5G base-stations, and 5G modems require having new antennas working at those frequencies. Not only this brings new challenges to the antenna design, but also it introduces new characterization requirements. In the last two sections of this research, to tackle 5G antennas characterization a novel near-field probe is designed, fabricated, tested, and used in a near-field measurement. The far-field radiation of an antenna under test is calculated based on the measured near-field. This setup can lower the characterization cost significantly while making it simple.

List of Figures

List of Tables

Table of Contents

1 INTRODUCTION

1.1 Motivation

Every decade with advancements in technologies new opportunities become available to scientists and public. Gradually, those technologies get integrated into academia, industry and life and take place of conventional solutions. For instance, before invention of printers, people used to use typewriters. When printers came to the market, taking advantage of widely accessible personal computers, printers became popular and turn out to be part of the routine life. It means after a while we get used to use printers as a normal tool for our tasks.

Nowadays, 3D-printers are paving the same path. Invention of 3D-printing was great news for innovators who could prototype and test their designs without having to make a vast upfront investment in manufacturing. The application of 3D-printing started from prototyping simple structures, then went through industries, but now, there is no end to it. In Section 1.2, the reason why we start with 3-D printing in this research is discussed.

When a new technology is introduced, it brings in new values and applications. But it can also result in new challenges for the designers. Thinking of taking advantage of higher frequency bands for communications has been

around for decades. It is basically because of widely unused spectrum that can increase data rate based on the Shannon–Hartley theorem

$$C = B \log_2(1 + SNR)$$

Where C is channel capacity (related to data rate), B is bandwidth (Hz), and SNR is signal-to-noise ratio. 5G communication is taking advantage of using higher available bandwidth at frequencies above 24 GHz. Antenna design and characterization at such frequencies require new benchmarks as the frequency increased. In Section 1.3, I will elaborate on why new designs are needed and why 5G antenna characterization faced new challenges.

1.2 Why 3-D printing in microwave components and antennas?

3D-printing is the next generation of fabrication in many industries. From medicine to construction, art and jewelry, 3D-printing is finding its space and being used more and more. Antenna and microwave components fabrication includes different types of conventional fabrications such as CNC machining, or PCB manufacturing. Previously, 3-D printing has been used for fabrication of antennas, microwave components such as filters, and Fresnel lens. In this research, I started with investigating use of 3D-printers available at UW-Makerspace for the application of microwave and antennas. With this fabrication trial, airbrushing copper paint to the 3D-printed structures is evolved. When I get

the confidence that this method works, I expanded the view and designed power-dividers and filters based on WR-90 waveguide standard. Testing each part showed acceptable results, while the component was made of light materials rather than bulk copper, and it was printed with a low-cost. These amazing potentials can be utilized in different applications specially, when there is a need for building a subsystem.

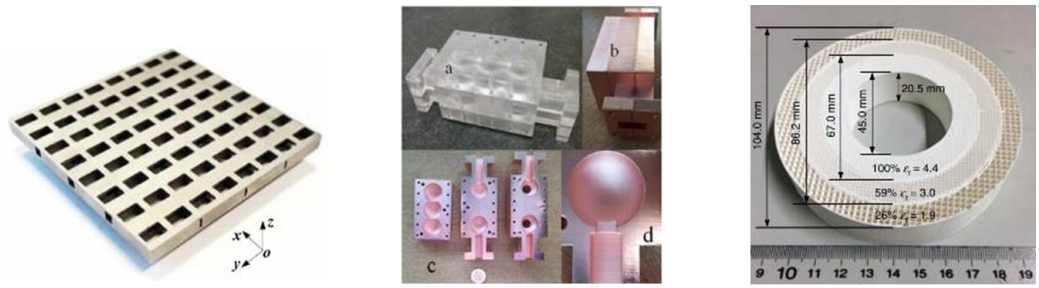

(a) (b) (c)

Figure 1.1 3-D printing applications in microwave and antennas. (a) 8×8 slot antenna array [1], (b) X-band filter based on 5 spherical resonators [2], (c) Fresnel zone plate lens [3].

Next, it was the time for antenna design to get inspired by this technique. There are more benefits to 3D antennas rather than planar antennas. With one more dimension, there is more control on radiation mechanism of the antenna, therefore, the antenna can be designed with improved performance. While the goal was to take advantage of 3D-printing in antenna design, I was looking for designs that are hard to fabricate with conventional methods. The Marchand-

balun integrated into a dipole antenna was an example for this idea. Later, I explore design of a leaky-wave antenna with 3D-printing, and a high-directive horn antenna with suppressed back-radiation. At the end, this fabrication technique helped design of the near-field probe and the measurement setup.

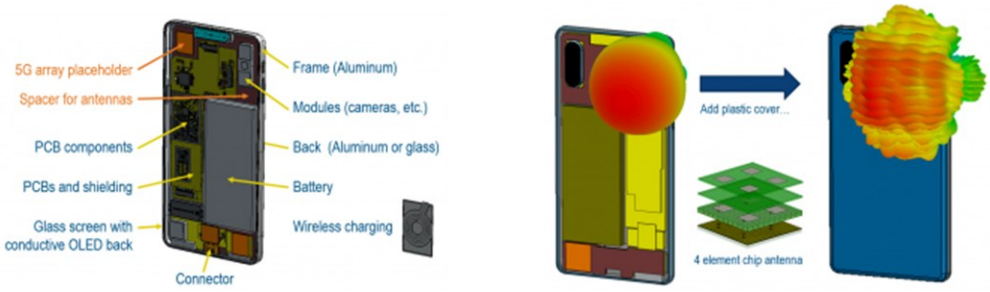

(a) (b)

Figure 1.2 5G antenna design challenges. (a) limited space for antennas next to different modules, and (b) substantially affected radiation pattern by plastic cover [4].

1.3 Why we need innovation in near-field antenna measurement?

While we always think of new methods to build a design, such as using 3D-printing, we should also have a look at new methods of characterization. Otherwise, conventional measurement methods limit us in evaluation of the designs and slow down innovation speed. Recently, the next generations of communications, 5G and even 6G, are getting lots of attentions among scholars and industries. 5G devices are getting into market and soon, a huge number of 5G

devices will be distributed to the world. From 5G phones to 5G modems, and 5G base-station antennas will include antennas that will cover the new frequency bands specified for 5G. Those frequencies are above 24 GHz, which are called FR2 band for 5G.

Antenna design for 5G frequencies brings new challenges for the antenna engineers. It is because that at FR2 band the wavelength becomes relative to the small dimensions inside the device, so the surrounding area of the antenna can impact the performance significantly (Figure 1.1 (a)). For instance, in a cellular phone, battery, screen, camera, and even the RF circuits can interfere wave propagations of the antenna. On the other hand, path loss increases by increasing the frequency, therefore, antenna designers should design 5G antennas in a way that use the power more efficiently. It is where directional antennas become interesting for the designers so that the power will be transmitted only to the desired directions. Therefore, there is a need for a beamforming system such as a phased-array antenna. All these together means that by introducing 5G, antenna design needs to change fundamentally in 5G devices. The new complexities introduced to the 5G antenna design brings new challenges for the antenna characterizations. As 5G antennas are very small and highly integrated into circuits, direct access to them for conducted testing is not practical anymore. Therefore, over-the-air antenna measurement techniques are needed to characterize the antenna performance. In the last two sections of this dissertation,

a new near-field probe and a measurement setup using that probe are discussed to simplify antenna characterization. The design is fabricated and tested at X-band as a proof of concept.

The published journal and conference papers from the accomplished tasks in this project are listed as follows:

- “3D-printed High-Directivity H-plane Horn Antenna with High Front-to-back Ratio Using Soft and Hard Walls”, Mohammadreza Ranjbar Naeini, and Daniel van der Weide, IEEE RWW 2021, San Diego, CA, USA (Virtual Conference)
- “High-Performance Probe for Over-the-Air Measurement”, Mohammadreza Ranjbar Naeini, Yuchen Gu, and Daniel van der Weide, 95th ARFTG, Virtual Conference, IEEE Microwave Week 3MT M/C choice winner
- “Monolithic 3-D-Printing of an Integrated Marchand Balun with a Dipole Antenna”, Mohammadreza Ranjbar Naeini, Mirhamed Mirmozafari, and Daniel van der Weide, IEEE Transactions on Components, Packaging and Manufacturing Technology, 2020
- “3-D Printed Frequency-Scanning Antenna with Suppressed Open-Stopband” Mohammadreza Ranjbar Naeini, and Daniel van der Weide, IEEE RWW 2020, San Antonio, TX, USA

- “A Low-cost and Compact X-band Near Field Antenna Measurement System” Mohammadreza Ranjbar Naeini and Daniel van der Weide (Abstract) IEEE APS/URSI 2019, Atlanta, GA, USA
- “Cascaded 3D-Printed X-band Components for Subsystems” Mohammadreza Ranjbar Naeini and Daniel van der Weide, IEEE Microwave and Wireless Components Letters, 2019

2 Assessment of 3D-printing in Microwave and Antennas

2.1 Introduction

The 3-D printing is a quick and cost-effective alternative to the traditional micro- and millimeter-wave component fabrication methods [5], and [6]. Recently, high-resolution 3-D printing is often the first choice for prototyping in many fields including dentistry. Likewise, fabricating waveguide components and antennas in a fast and cost-effective method using plastic and then coating them using conductive materials could enable applications for which structure complexity inhibits traditional methods of fabrication, and the insertion loss does not need to be as low as bulk copper. Among different 3-D printing technologies, fused deposition modeling (FDM) and stereolithography (SLA) are most accessible.

Various 3-D printed waveguide components and antennas have been reported, such as bandpass waveguide filters [7], [8], horn antennas [6], [9] a parabolic dish reflector antenna [8], and a passive front end [10]. To use a 3-D printed waveguide component, at least the inner surfaces should be conductive enough to guide the wave. One solution is to print the entire object in copper, though this is costlier than the traditional machining when the component requires large amount of material. Another solution is plating a conductive material on surfaces of 3-D printed object in plastic using a chemical process [7], [6], [11], but a simpler method is coating conductive paint [9], [12].

In this chapter, we investigate a metal painted plastic (MPP) method by using copper paint on 3-D printed waveguide components, starting with a comparison between straight sections realized in two different processes. Although printing in FDM is less expensive than SLA, SLA has better resolution. Because FDM and SLA are readily available, the first prototypes are fabricated with these technologies and the results are compared. Then, we design, fabricate, and measure an iris-coupled bandpass filter and a power divider. Finally, the fabricated parts are cascaded, and the comparison shows the possibility of building a subsystem. Building a subsystem from components allows us to print parts simultaneously in different printers, redesign, and replace any required component without changing others.

2.2 SLA and FDM Performance Comparison

To compare processes, we print two 127-mm straight waveguides at X-band (WR-90 standard) with SLA and FDM as shown in the inset of Figure 2.1. The same resolution of 25 μm is used for printing in FDM using an Ultimaker printer and SLA using a Form2 printer. Acrylonitrile butadiene styrene (ABS) is selected for printing in FDM, and the “Durable” material [13] is selected for printing in SLA, as it does not warp after printing. Standard flanges (UG-39/U)

are added to the 3-D models of waveguide parts to be compatible with measurement tools.

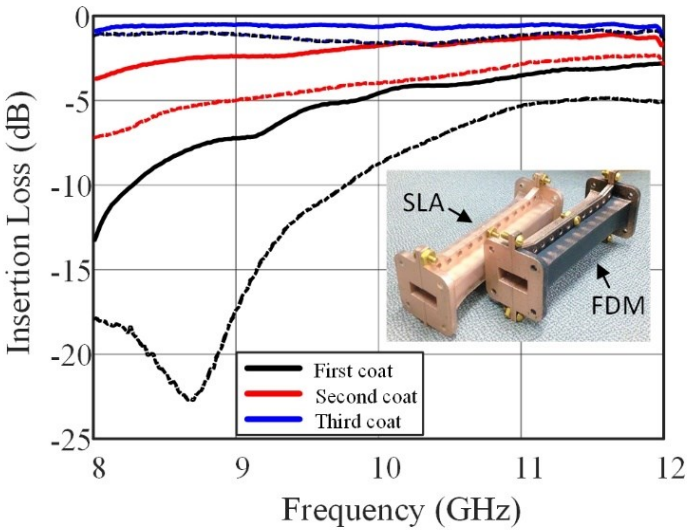

Figure 2.1 Insertion loss improvement after each coat on FDM-printed waveguide

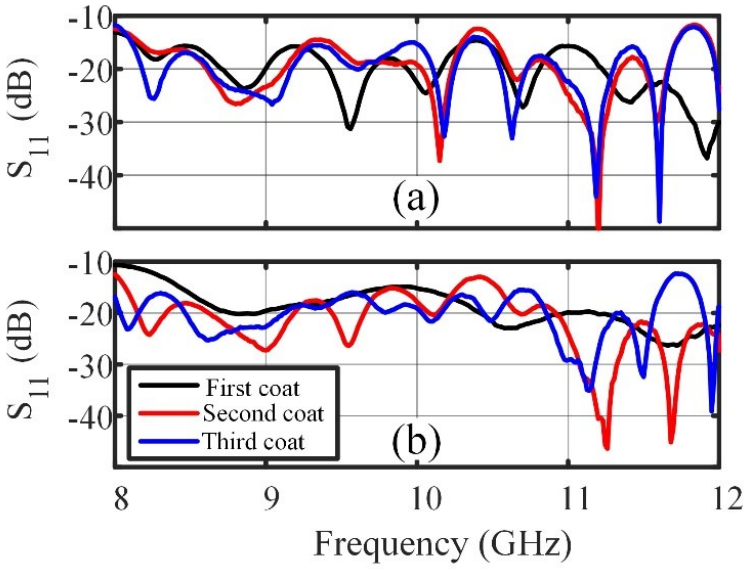

Figure 2.2 Input reflection coefficient of the printed coated waveguides. (a) SLA. (b) FDM.

To paint all of the internal surfaces, the 3-D waveguide model is made in two halves. We cut the model along the E-plane on the larger dimension of the waveguide since the surface current along this line is zero. Therefore, the unavoidable gap has minimum loss upon connecting the halves using screws. To render inner surfaces conductive, each waveguide is painted three times using Caswell copper conductive paint [9], and measured after each coat. The copper paint includes water, copper, titanium dioxide, silver, carbon black, and cyclic amine, where about 25%–30% of the paint is copper [14]. The conductivity is measured with the four-point probe method and verified in an electromagnetic simulation using the CST. The measured bulk conductivity is 6×10^4(S/m). Scattering parameter measurements are plotted in Figures 2.2 (a) and (b), showing improved reflection coefficients and lower insertion loss after each coat. The main reason for this improvement is that the copper thickness is approaching the required skin depth, which is estimated to be between 60 and 70 μm at 10 GHz. Insertion loss of the final waveguides is compared with commercial copper waveguide in Figure 2.3, which shows an average of 3.1 and 6.3 dB/m penalty in X-band for SLA and FDM waveguides, respectively.

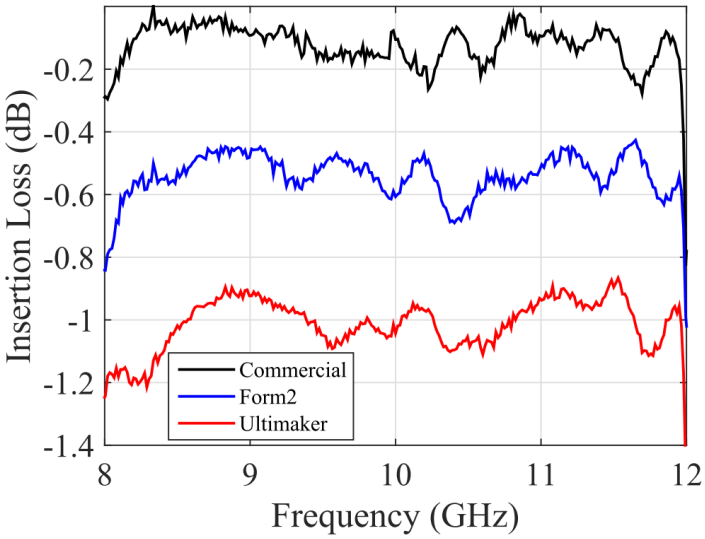

Figure 2.3 Insertion loss comparison of a 127-mm-length commercial waveguide

To investigate the causes of losses, the layers thickness and surface roughness are measured using a 3-D optical metrology system (Alicona InfiniteFocus with Real3D). Figure 2.4 (a)–(c) show the measured thickness of coated copper after each paint, which are 24, 44, and 72 μm.

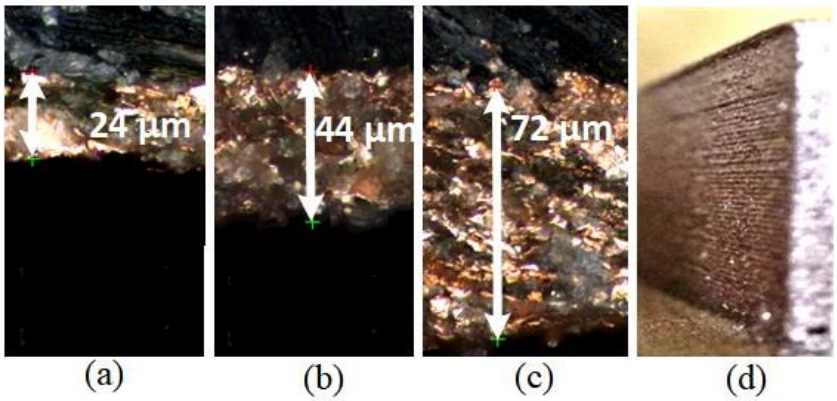

Figure 2.4 Coated layers thickness measurement. (a) First coat. (b) Second coat.

Table 2. 1 Measured R_a (µm) and R_q (µm) of coated 3D-printed samples.

	R_a (FDM)	R_q (FDM)	R_a (SLA)	R_q (SLA)
1st coat	5.4	6.9	3.9	5
2nd coat	5	6.4	3.8	5
3rd coat	4.7	6	3.7	5

The average surface roughness values *Ra*, defined as average height of selected area, and $\boldsymbol{R_q}$, defined as root-mean-square height of the selected area, of different samples printed horizontally and painted under the same procedure are measured after each coat and summarized in Table 2.1. Surface roughness of 5 μm is inherent in the paint. The surface roughness for SLA samples is better than FDM, but the difference is negligible. In FDM, vertically oriented surfaces during the printing have anisotropy in the layering direction, inversely related to printing resolution, leading to surface waviness (Figure 2.4 (d)). Thus, insertion loss penalties are a combination of copper paint and the gap between two halves. In addition, the surface waviness in FDM prevents full paint acceptance on the surfaces giving more loss in comparison to SLA; thus, we produce a bandpass filter and a waveguide power divider in X-band using SLA and the same coating procedure in this chapter. Table 2.2 shows the comparison of the results of rectangular waveguides fabricated and metalized using different methods with

this work. It shows that an acceptable insertion loss is achieved while the fabrication process is simple, fast, and cost-effective.

In stereolithography (SLA) 3D printing, liquid resin is cured by a highly-precise laser to form each layer, which can achieve much finer details and is more reliable to repeatedly achieve high quality results. And based on [5], the SLA method for 3D printing that was used in this paper is one of the best in terms of accuracy. The tolerance in dimensions is less than %0.3 (reported in [5]), therefore, its effects should be negligible in the device performance considering the 3D printing constraints like minimum gap size, maximum overhang length, minimum supported wall thickness, and so on [6]. The estimated effect based on CST simulations is a very small shift in the device bandwidth.

Table 2.2 Loss Comparison of different 3D printing and metallizing of rectangular waveguides

Waveguide Standard	**Technology**	**Material**	**Loss (dB/λ_0)**	**Frequency (GHz)**	**Ref.**
WR90	SLA	Conductive Painted Durable material	0.11	10	This work
WR90	FDM	Conductive Painted ABS	0.2	10	This work
WR90	Machining	Copper	0.012	10	[7]

WR90	FDM	Copper plated ABS	0.013	10	[7]
WR62	FDM	Conductive PLA	8.07	13	[8]
WR42	FDM and ink dispensing	Sliver ink coated ABS	0.478	22.25	[9]
WR4	CAM	Copper	0.054	215	[10]

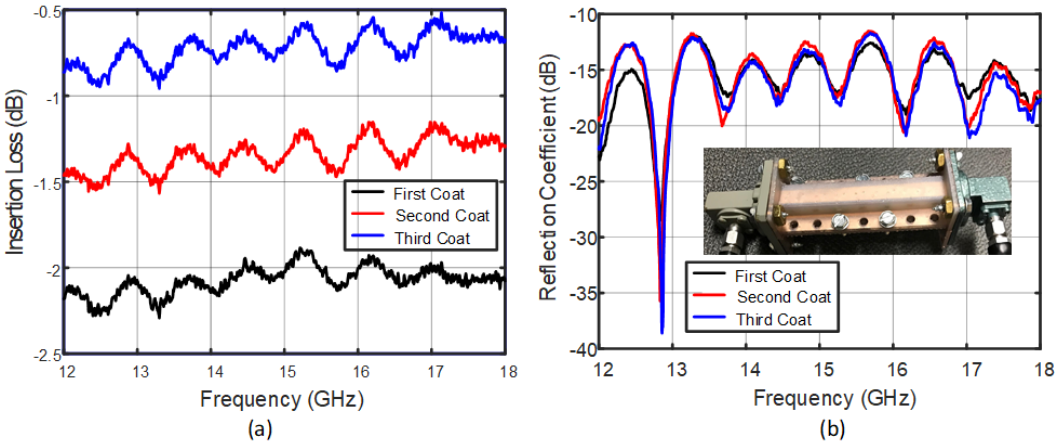

Figure 2.5 Results of a 3D printed Ku-band rectangular waveguide after each coat. (a) Insertion Loss, (b) Reflection Coefficient. The inset is the fabrication and coated Ku-band rectangular waveguide.

To evaluate this method in higher frequencies the same waveguide component prototyping is done by 3D printing a rectangular waveguide at Ku-band (12-18 GHz) and coating with the same procedure. The results plotted in the

Figure. 2.5 show acceptable insertion loss and reflection coefficient for a low-cost and fast fabrication method while the waveguide is coated three times.

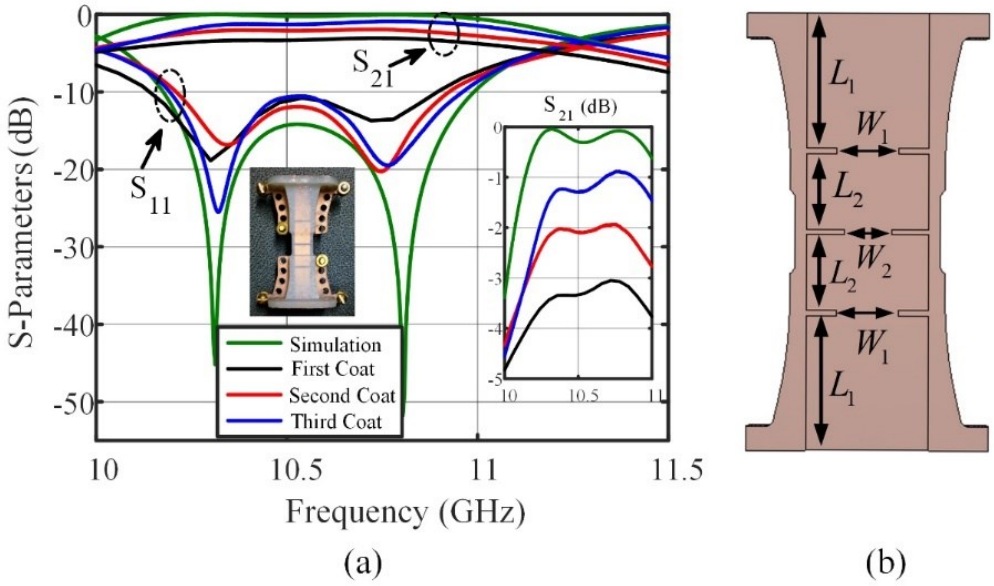

Figure 2.6 (a) Iris-coupled bandpass filter designed dimensions: L1 = 25 mm, L2 = 14 mm, W1 = 11.4 mm, and W2 = 8.8 mm. (b) Simulated and measured scattering parameters comparison of the iris-coupled bandpass filter (inset is the fabricated filter).

2.3 Bandpass Filter and E-Plane Power Divider

Microwave filters are essential in communications systems. Here, we use the impedance inverter model [15] to design a two-pole iris-coupled rectangular waveguide bandpass filter. The center frequency is set at 10.5 GHz with 8% bandwidth. After designing the filter, its performance is verified using CST

Studio, and then the model exported to be 3-D printed. The thickness for each iris wall is set to 1 mm, and other dimensions are labeled in Figure 2.6(a). The filter is printed using SLA with the same coating process. Figure 2.6 (b) shows the fabricated filter and its scattering parameters of the simulation and measurements. The measurement results show that successive coats give ~ 2.1-dB improvement in insertion loss, approaching bulk copper.

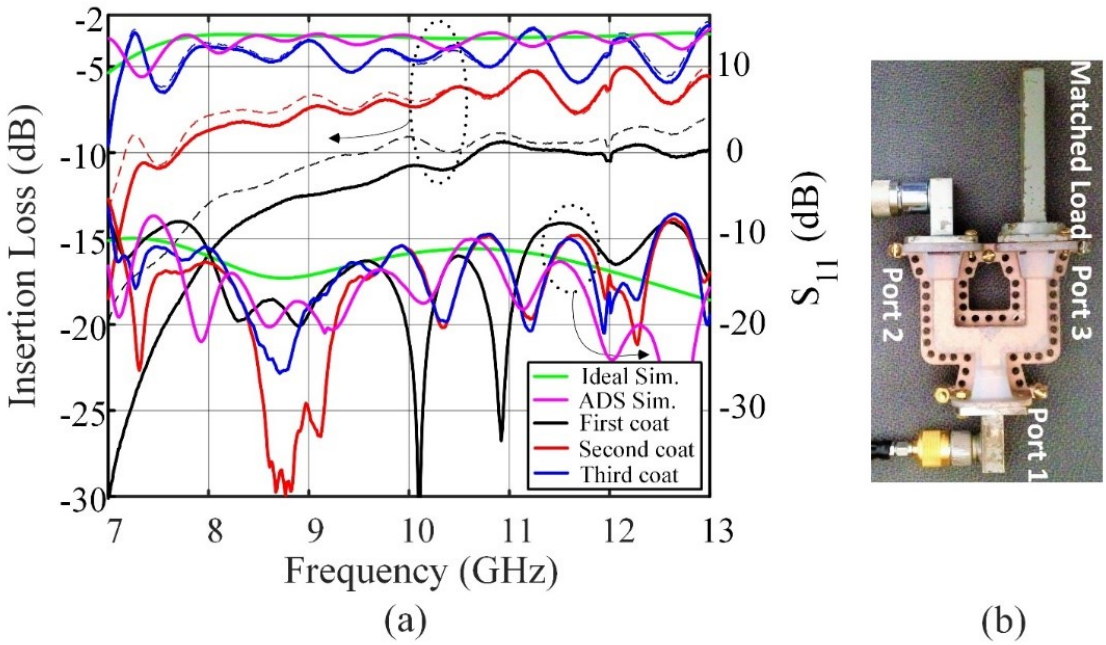

Figure 2.7 (a) Simulated and measured insertion loss (S21 is the solid line and S31 is the dashed lines) and reflection coefficient (S11) of the power divider. (b) E-plane power divider in the measurement setup.

Finally, we fabricate a rectangular waveguide power divider. To cut the waveguide where the surface current is zero, an E-plane power divider is selected.

The measurement results in Figure 2.7 (a) show that the 3X coated power divider has 7-dB improvement in insertion loss at 10 GHz, with average -0.5 dB over X-band versus simulation. The insertion losses of both paths are similar, independent of painting. Figure 2.6 (b) shows the fabricated and coated power divider with one of the output ports connected to a matched load. The same nonideal matched load is used in an ADS simulation. It shows that the ripples in the measured insertion loss are due to the reflected waves returning from the nonideal matched load.

2.4 Cascade of the 3-D Printed Components

To show that 3-D printed waveguide components can be cascaded to build a subsystem, we connect the fabricated components in Sections 2.1-2.3, as shown in Figure 2.8, measure the insertion loss, and compare to the simulation of the same cascade. The results show good agreement between reflection coefficients and average 1.2 dB of insertion loss within 0.1 dB of the sum of penalties of each. It proves that with this method we can overcome practical limitations of fabrication sizes in 3- D printers and make a lightweight and low-cost system while not adding significant loss.

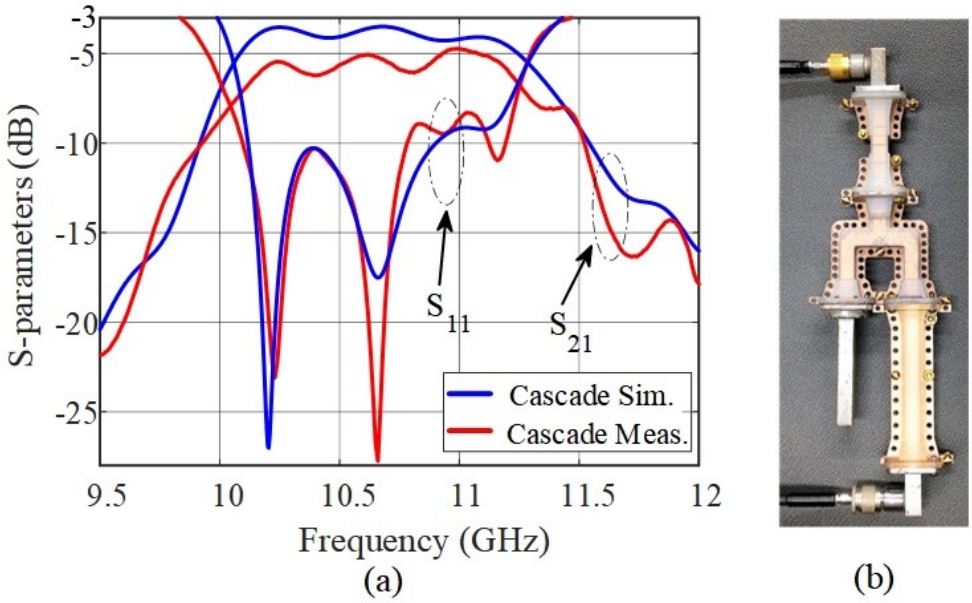

Figure 2.8 (a) Insertion loss and input reflection coefficient comparison between the measured and simulated cascaded waveguide components. (b) Cascaded 3-D printed X-band waveguide components

2.5 Conclusion

In this Chapter, two popular methods of 3-D printing, SLA and FDM, are chosen for building low-cost and lightweight microwave components. Conductive paint is used for coating layers of copper on the inner surfaces. The results of straight waveguides show that SLA has a better performance. Results verify that a microwave subsystem can be printed and painted separately, then cascaded. This idea could be generalized at higher frequencies where the components are smaller.

3 Tackling Challenges in Monolithic Fabrication of Antennas with 3D-printing

3.1 Introduction

Recent advancement in manufacturing technologies has facilitated the fabrication of complex geometries. Using 3-D printing, fabrication is low cost, fast, and could be environmentally friendly [16]. More importantly, additive manufacturing can overcome some of the limitations of traditional fabrication methods, such as creating small interior features. This potential has been demonstrated in some fabrication of 3-D antennas [17], [18], [19], [20]. While 3-D printing simplifies the fabrication process, monolithically printing a structure is always a challenge due to the requirement for supports at places where there is no access for removing them. In [21], methods for avoiding supports are discussed, such as rotating the structure in order to be vertically aligned, so the structure can support itself. However, not all of the structures are able to be self-supported. In addition, conductive coating has been always problematic [22], [23]. It is more challenging if an internal surface of an antenna is to be metal coated. Some solutions have been proposed to address this issue [24]. In many of them, the RF device has been split into two equal pieces to access internal features [25], [26]. This is not a convenient solution since it prevents the monolithic fabrication of an antenna.

In this chapter, first, a fast 3-D printed prototyping method that preserves antenna integrity both in fabrication and copper coating is presented. As an

example of nonplanar architecture with internal features, a Marchand balun integrated with a dipole antenna has been 3-D printed. A variation of that Marchand balun has been adopted to enable its 3-D printing fabrication. This modified Marchand balun results in a shorter feed line. The antenna was fabricated monolithically *in situ*, in a single run, simplifying the assembly process. The conductive coating was realized by airbrushing the antenna using a metal painted plastic (MPP) method [27]. Some cutout windows are embedded into the design providing access to the interior surface of the antenna for airbrushing. These cutouts are considered at specific regions where the power flows are minimum, and hence, they do not affect the antenna performance. This fabrication method enables fast and efficient prototyping of nonplanar complex geometries with commercially available printers.

3.2 Antenna Structure with Introduction of Cutout Windows

The proposed antenna was initially designed as an easy-to-fabricate alternative to the dipole antenna in [28] for multifunction radar. The antenna geometry is shown in Figure 3.1. A portion of the front wall is removed to show the Marchand balun geometry. The feed lines are hollow using air as the dielectric. Originally, the Marchand balun was introduced with an open-circuit stub [29]. An open-circuit stub can be replaced by a short-circuit stub with a $\lambda/4$

shorter length. This results in common-mode resonance rejection [30] and a more compact feed line. We exploit this variation to realize the 3-D printed fabrication of the Marchand balun. The short-circuit point, referenced in Figure 3.1, first provides a supporting point for the ɾ-shape structure to keep it inside the feed line. Second, the holes close to this point provides access to the interior of the design. This allows for various types of conductive coating, including electroplating and airbrushing. The electroplating fluid or copper paint can penetrate the geometry through these holes via the short-circuit point. The balun is integrated into a dipole antenna standing a $\lambda/4$ above the ground plane. Some cutout windows are embedded into the outer surface of the antennas to provide access to the interior space of the antenna. These cutout windows facilitate copper coating of the antennas using either airbrushing or electroplating.

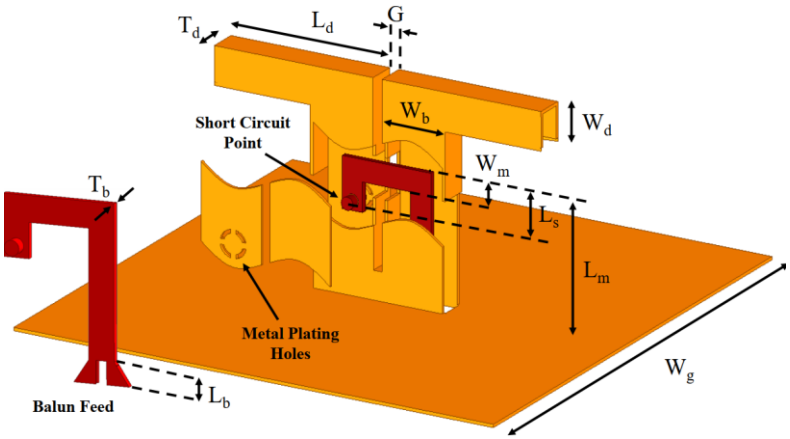

Figure 3.1 Structure of the proposed antenna. A portion of the front wall is separated to represent the inside feed line. The antenna has a hollow structure.

To precisely locate these windows, the power flow distribution on both inner and outer surfaces of the antenna is simulated and shown in Figure 3.2. The encircled windows carry power -40 dB lower than 0 dB input power. Therefore, cutting these windows away will not affect antenna performance. This will also be verified later in the measurement section. Like the original Marchand balun, the proposed balun provides an impedance transformation from an unbalanced input impedance (50 Ohm) of the stripline to a balanced output impedance (~70 Ohm) between two extensions of the outer conductors [29]. While the width of the -shape conductor (W_m = 3.4 mm), its thickness (0.8 mm), and its clearance from the outer conductor (1.5 mm) determine the former impedance, the 70- impedance is adjusted by the gap between two outer conductors (G) and their widths (W_b). This balun has two intrinsic resonant frequencies, providing the antenna with a wideband characteristic [29].

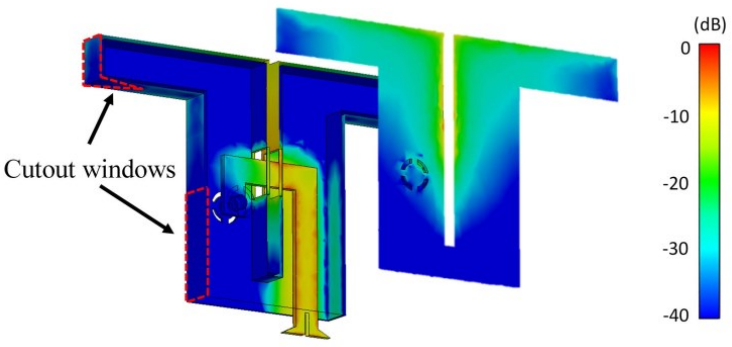

Figure 3.2 Power flow distribution on inner and outer surfaces. Dashed lines show areas that carry negligible power. The simulation shows that removing these areas does not affect antenna performance.

The resonant feature of the proposed antenna can be adjusted over a wide range of frequency with desired bandwidth. Figure 3.3 (a) and (b) demonstrate this capability by a parametric study on the length (L_d) and the width (W_d) of the dipole antenna. As shown, the length of the dipole can be primarily adjusted to obtain the resonance frequency. Then, the bandwidth can be optimized by fine-tuning the length and the width of the dipole simultaneously. This feature makes the proposed antenna an appropriate solution for various applications at a different frequency range.

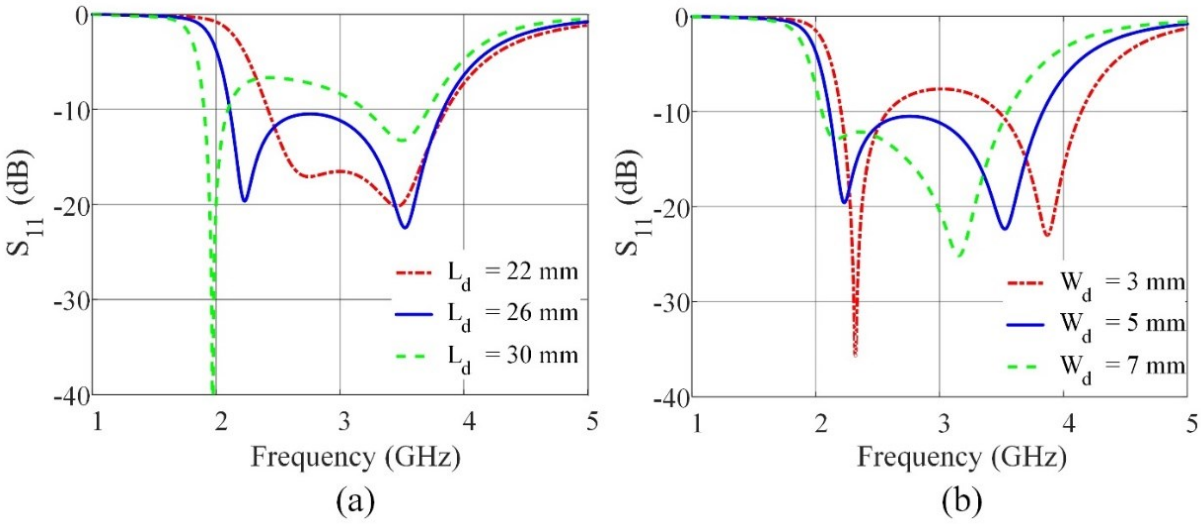

Figure 3.3 Parametric study of the antenna dimensions. (a) Variation in antenna length (Wd = 5 mm). (b) Variation in antenna width (Ld = 26 mm).

The antenna parameters were optimized considering the center frequency and the bandwidth, and its final parameters are provided in Table 3.1.

Table 3. 1 Detailed dimensions of the fabricated dipole antenna with integrated Marchand balun. (Unit: mm)

W_m	L_d	W_b	W_d	G	T_d	L_s	L_m	W_g
3.4	26.5	10.5	2	1.5	4.8	8	22	80

3.3 Fabrication Process

The fabrication steps for the proposed antenna are shown in Figure 3.4. The whole structure, including the ground plane, the balun, and the dipole, is monolithically fabricated in a single run. A commercially available 3-D printer, Ultimaker 3, was used in this fabrication, costing less than $1 per antenna for the materials. To handle overhangs, support structures, as shown in Figure 3.4 (a), were simultaneously fabricated both inside and outside of the geometry with antenna layers. To reduce the amount of polyvinyl alcohol (PVA) used in the 3-D printing, the support structure is optimized using Ultimaker Cura, the printer's software. These supports enable 3-D printing of nonplanar antennas with internal features. Removing supports is often problematic in complex geometries where there is no access to interior spaces [21], no rotation of the structure would avoid supports, and a redesign to be a self-supported structure is impractical. To solve this problem, PVA, which is water-soluble, was selected. The best match with

PVA is polylactic acid (PLA), which is made from renewable resources and environmentally friendly [16].

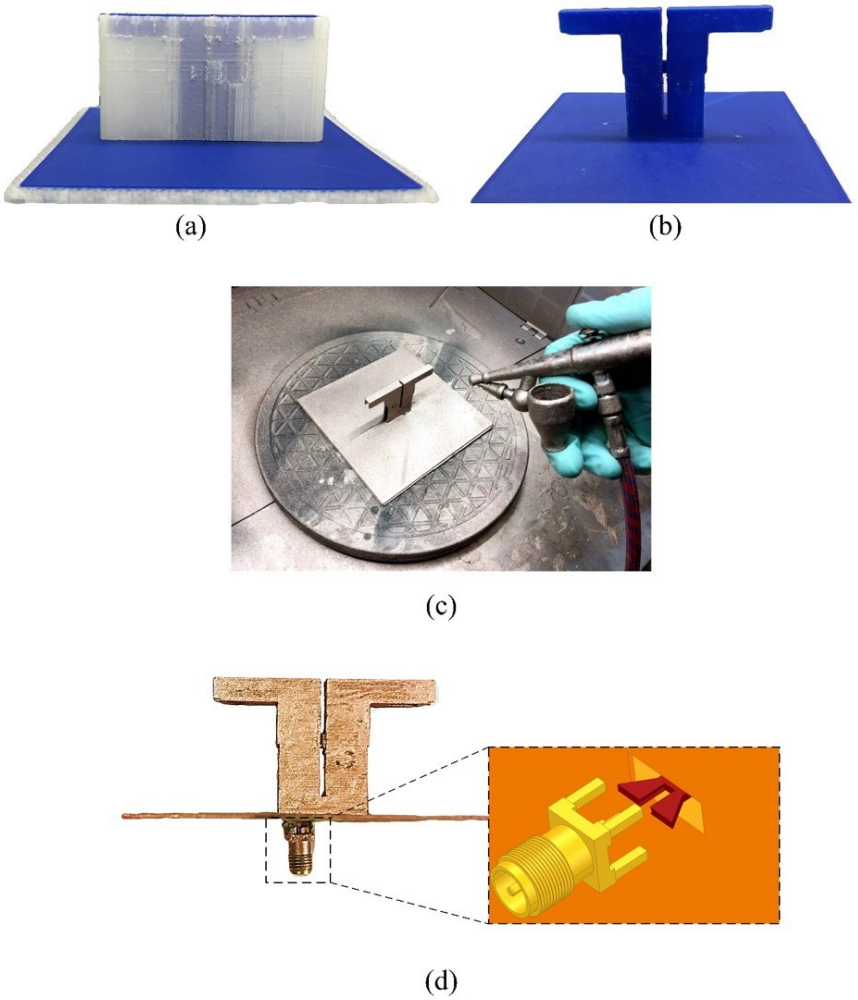

Figure 3.4 Antenna prototype after each fabrication step. (a) 3-D-printed prototype with the support structure. (b) Antenna after dissolving the supports. (c) Final antenna after copper painting and soldering an SMA connector. The inner conductor extension and its cutout are magnified in the subset. (d) Conductive coating the 3-D printed antenna via airbrushing.

The fabricated prototype after removing the PVA supports is shown in Figure 3.4 (b). Finally, the interior and exterior surfaces of the structure were airbrushed using the Caswell copper-conductive paint shown in Figure 3.4 (c).

Compared with other conductive coating methods, airbrushing is fast, cost-effective, and reliable. An electroplated 3-D printed dipole, for example, is discussed in [28]. The preprocessing of the antenna in electroless fluid followed by the thick copper deposition in high current causes deformation of both the dipole and the ground plane. This degrades the antenna polarization purity. To resolve this issue, we proposed a fast airbrushing method that does not disturb the antenna geometry. To do the copper deposition via airbrushing, one needs a source of pressurized inflammable gases, such as air or nitrogen. A regulator, mounted on the outlet valve of the tank, adjusts the gas pressure. The typical pressure used in this project was 40 psi. The distance to the antenna shell during the airbrushing was about 20 cm, and the deposition time was optimized to get about 25-μm thickness on outer surfaces after each round of painting. To airbrush internal surfaces, the airbrush nozzle needs to get closer to the windows to push copper paint into the geometry. After repeating this procedure, a couple of times, a sufficient conductive coat covers the whole internal surfaces. In this work, the antenna was coated twice. The average surface roughness (R_a) of the painted structure is 5 μm. It is worth mentioning that there is no need for any treatment to avoid adhesion. A reliability test is done after several months of airbrushing

the same copper paint on the surfaces of some 3-D printed plastic waveguides. The result did not show any degradation in the performance since the materials included in the formula of the copper paint protect it from corrosion. A commercial SMA connector is used to launch into the stripline. Figure 3.4 (d) shows the final prototype of the proposed antenna after assembling the connector. To facilitate the connector assembly, the centerline is slightly extended. This modification is shown in the inset of Figure 3.4 (d). In addition, a cutout equal to the size of the SMA inner pin is inserted at the beginning of the feed line. This provides a convenient platform for connector assembly. The outer four legs of the SMA connector are soldered to the ground plane. To prevent any damage to the 3-D printed structure due to the soldering, the attachment should be done fast and at low temperatures. Conductive paste can alternatively be utilized to assemble the connector.

3.4 Measurement Verification

To compare the simulation results with the measurement, a conductive material is defined in CST Studio with the measured conductivity of the copper paint [6×10^4(S/m)] [12]. The reflection coefficient of the fabricated prototype was measured using an Agilent N5230A Network Analyzer. The calibration was done using an Agilent N4694A E-Cal in which the reference plane is the end of

the measurement cable. The measured S_{11} is compared with simulation in Figure 3.5. The simulation of the antenna with and without the cutout windows shows the negligible deviation of S_{11}. The measurement result matches well to that of simulation, having S_{11} < -10 dB over a wideband frequency range from 2.12 to 3.95 GHz. The result verifies the reliability of this specific 3-D printing fabrication and copper painting.

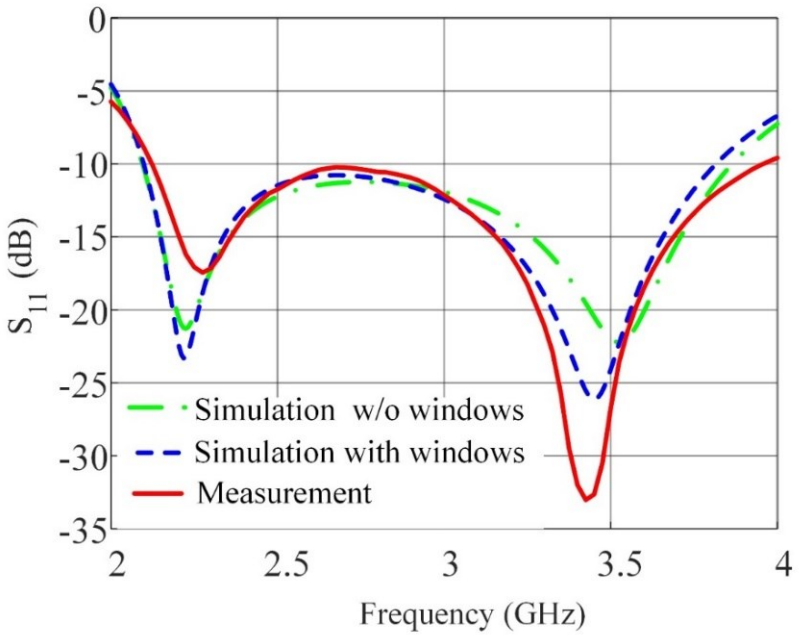

Figure 3.5 Measurement verification of the simulated S11 with and without cutout windows.

Then, the realized gain of the fabricated antenna was measured and compared with the simulation results of the antenna with and without the cutout windows in Figure 3.6. The simulation shows that the cutout windows do not affect the realized gain. The measured gain has acceptable performance

comparing to the simulations. The slight variations of the realized gains are due to the ground plane constructive and destructive diffractions that the result of the measurement setup. It is worth mentioning that the same antenna fabricated in pure copper would have about 1 dB higher gain due to the conductivity [30].

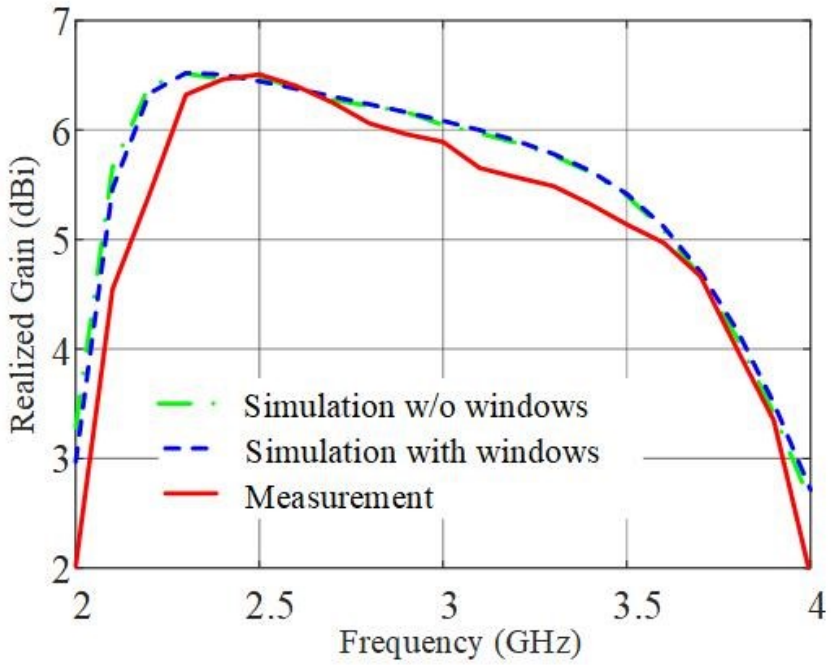

Figure 3.6 Comparison of realized gain of the antenna among the simulation with and cutout without windows and the measurement.

The radiation patterns of the antenna were measured in an anechoic chamber. The radiation characteristics were verified at three different frequencies across the operational bandwidth in both E- and H-planes in Figure 3.7. The measurement results show a co-polarization to cross polarization better than 30 dB in both principal planes. This is slightly lower than the simulation results, which may be due to fabrication tolerances and diffractions of the measurement

components. An increased back lobe is also shown in the radiation patterns. This back radiation is due to the feed-line extension. It was verified in simulation, but the results are not provided for brevity.

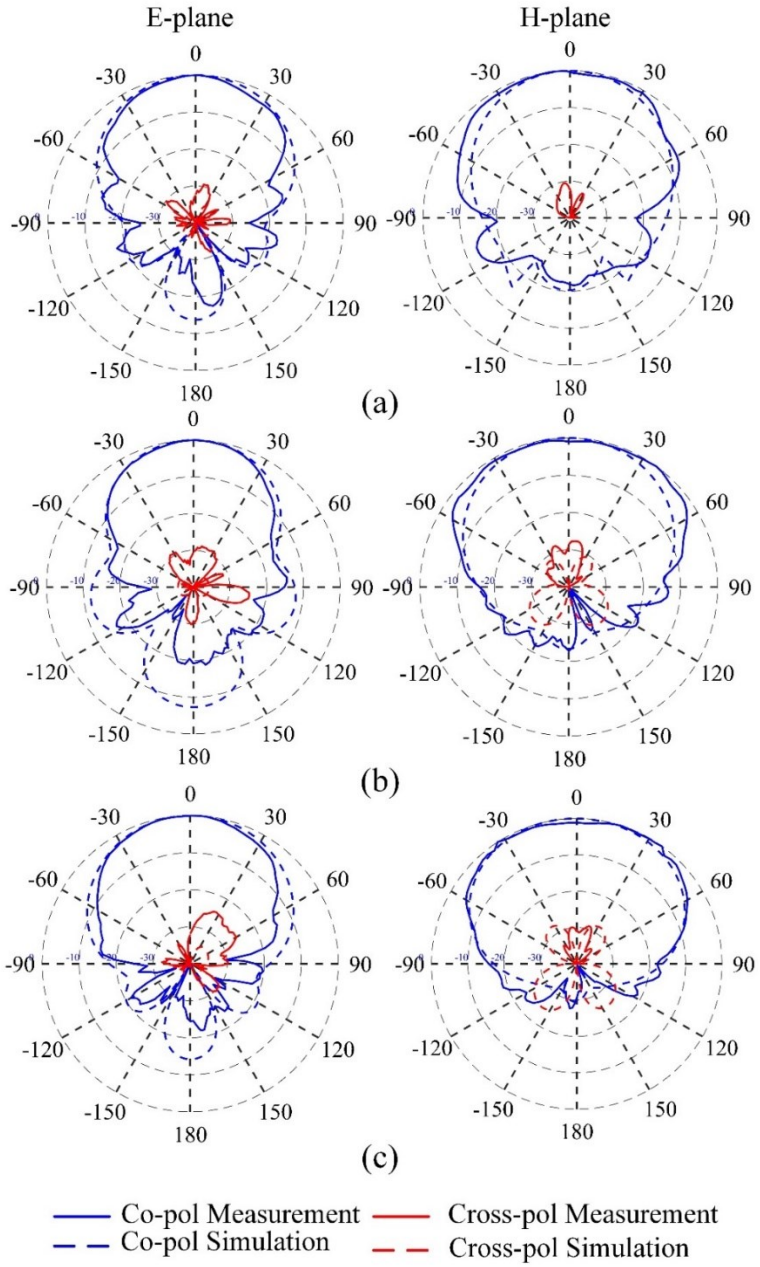

Figure 3.7 Measured and simulated radiation patterns of the proposed antenna at principal planes at (a) 2.2, (b) 3, and (c) 3.5 GHz

3.5 Conclusion

A fast 3-D printed prototyping method of integrated antennas with internal features was presented in this chapter. This fast prototyping includes modifications both in fabrication and metal coating. As a proof of concept, a Marchand balun integrated with a dipole antenna was prototyped. Using soluble materials, the supports were printed, which can be easily removed afterward. This preserves the original design of the antenna eliminating the need for additional rotation or change in the structures. Cutout windows, on the antenna external walls, are introduced to facilitate copper paint airbrushing. It has been verified that careful adjustment of these windows does not affect the antenna performance. The fast prototyping methods, discussed in this study, can be applied to other complicated antennas with internal features, opening the door for future research activities.

4 NOVEL WAVEGUIDE ANTENNAS BASED ON 3D-PRINTING

4.1 Introduction

In every industry, there are some conventional fabrication methods that are being used for years without any revolution. Over the years, some new features are added to them, while keeping the base fixed. In electronics and antennas, PCB technology dominated the industry. Every circuit board, and most of the antennas are designed based on PCB stack-up. This is mainly because of integrating antenna and circuit in a single PCB. Microstrip line, substrate-integrated-waveguide (SIW), and co-planar waveguide, are the well-known types of media based on PCB which are being used for antenna design. But antenna design based on PCB suffers from PCB dielectric loss and being limited to a planar design. A more efficient and compact antenna can be designed based on 3 dimensions rather than 2 dimensions. Waveguide-based antennas such as a horn antenna or slotted waveguide antenna are examples of 3D antennas. Since they are hollow structures, they do not lose power due to dielectric loss. And, because of the 3D structure there is one more dimension of freedom for the antenna design. This flexibility can help solving some antenna design challenges.

In this chapter, two examples of 3D waveguide antennas designed based on unique features of 3D-printing. The first antenna is a Frequency Scanning Antenna (FSA). FSAs are desirable for low-cost beam-scanning over phased-array antennas. Some of the applications of FSA are imaging [31], radar [32],

[33], direction-of-arrival estimation [34], and weather measurement [35]. Design of an FSA can be done based on microstrip, substrate integrated waveguide (SIW), or rectangular/circular waveguide. Waveguide-based FSA is preferable due to the low loss it has vs. microstrip or SIW FSA. But fabrication of a complex waveguide-based FSA, specially at higher frequencies, e.g. mm-wave, is costly and challenging [36]. Traditional FSAs are unable to steer the beam to the broadside angle as an open-stopband occurs at the corresponding frequency and deteriorates the antenna gain [37]. Different solutions have been proposed to overcome this problem. For example, in [38], by asymmetrically designing the top and bottom slots of a leaky-wave antenna (LWA) based on substrate integrated waveguide spoof surface plasmon polariton the stopband is treated. In [39], by impedance matching the radiating element by its length in a meandered line microstrip FSA, the open-stopband is eliminated. And in [40], a collinear-slotted periodic LWA based on double-ridged SIW is proposed, in which by offsetting the SIW for each slot the impedance matching is achieved at the open-stopband. Fabrication of a waveguide FSA can be done by 3-D printing, which is a quick, accessible, and cost-effective alternative solution to the traditional fabrication methods. A waveguide structure can be 3-D printed in bulk metal [41], or in plastic. The inner surface of the plastic structure needs to be conductively coated. The latter solution is cost effective, as it can be done by using commercial low-cost 3-D printers and uses the least amount of conductor for realization of

the desired component or antenna [42], [43]. In section 4.2, the design of an FSA at X-band for symmetrical beam steering around the broadside is discussed. The open-stopband is completely suppressed by unique accessibility given by 3D printing. It was driven by designing capacitive and inductive posts inside the structure. The structure is fabricated using 3-D printing and conductive coating.

Then, to show another potential of 3-D printing for antennas, an H-plane horn antenna with high directivity and suppressed back radiation is designed, fabricated, and measured. High gain antennas are always of interest in different applications where there is a need for long range transmission such as satellite communications [44], [45], WLAN [46], and radar [47] or for short range communications at high frequencies (e.g. V-band) [48]. Horn antennas are some of the best candidates because of their simple geometry, wide bandwidth, and high gain. But bulkiness limits their applications. However, H-plane horns can overcome this drawback while maintaining benefits for antenna arrays [49] and substrate integrated waveguide (SIW) [50]. The invention of SIW technology has enabled fabrication of modified H-plane horn antennas. For instance, an arc shape is added to the SIW-based H-plane horn design to improve the radiation matching in [51]. By adding tapered vertical slots to the aperture of the H-plane horn, gain is improved in [52]. And by radially extending the dielectric to the front of the H-plane horn antenna (forming a semicircle) a lens is realized to perform as a phase corrector in [53]. Although these examples are realized using printed circuit board

(PCB) technology and benefit from that, they suffer from limitations of PCBs. First, dielectric loss of the substrate is inevitable. Second, SIW requires high precision fabrication at higher frequencies (mmwave), resulting in higher cost and less applicability to mass production. Third, it is difficult to drill metallic vias precisely around the edge of the substrate cut regions [50]. Finally, it limits the design to planar structures, preventing the benefits of 3D designs. To address the latter, one can use a multilayer substrate. A gradually decreasing ridge height inside an H-plane horn antenna based on SIW is designed in [54], but it makes fabrication difficult and increases the cost. As mentioned, the alternative to SIW technology is 3D-printing. It is quick and cost-effective while enabling high-resolution fabrication. It has been widely used in fabrication of novel antennas and microwave components with complex geometries [55], [56], [57]. In section 4.3, the design of the H-plane horn is discussed. By taking advantage of hard and soft walls, a high-gain and wideband H-plane horn antenna with high front-to-back ratio is designed and realized using 3D-printing. Design of such a 3D structure with horizontal and vertical details filled with air instead of dielectric but using 3D-printing material as the required dielectric in the design show the advantages of 3D printing.

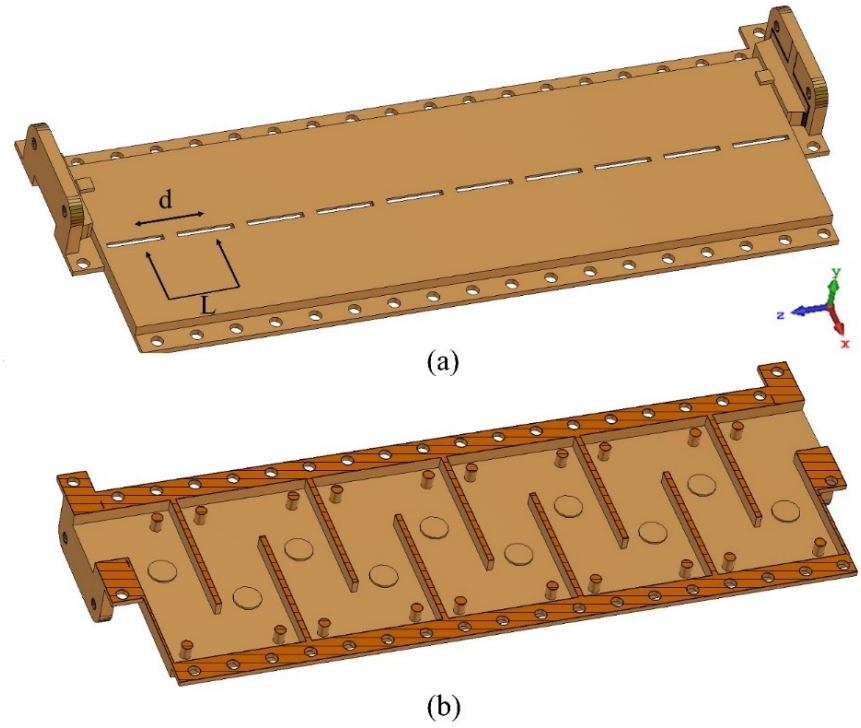

Figure 4. 1 The structure of the proposed frequency scanning antenna. (a) Upper half of the antenna, (b) Lower half of the antenna, which shows the meandered waveguide feed with posts.

4.2 Design of a Frequency-Scanning Antenna with Suppressed Open-Stopband

The Frequency Scanning Antenna proposed in this section is a slot array antenna consisting of 10 slots arranged in a line with spacing d = 24.8 mm, shown in Figure 4.1 (a), and a meandered waveguide feed, shown in Figure 4.1 (b). The meandered shape of the feed results in a higher scanning rate as the phase difference between two adjacent elements is proportional to the electrical distance between them. But the bends can result in high reflections if not treated. In an

FSA at the center frequency the electrical distance between two adjacent slots should be L= nλg/2, where *n* is a natural number and λg is the guided wavelength.

In this design, n = 2, and λg = 42.8 mm at center frequency, therefore, L = 42.8 mm. To suppress the open-stopband and match the bends, two inductive posts at the bends and one capacitive post with d_c distance before the slot antenna are designed in a unit cell of this antenna. The unit cell is shown in Figure 4.2.

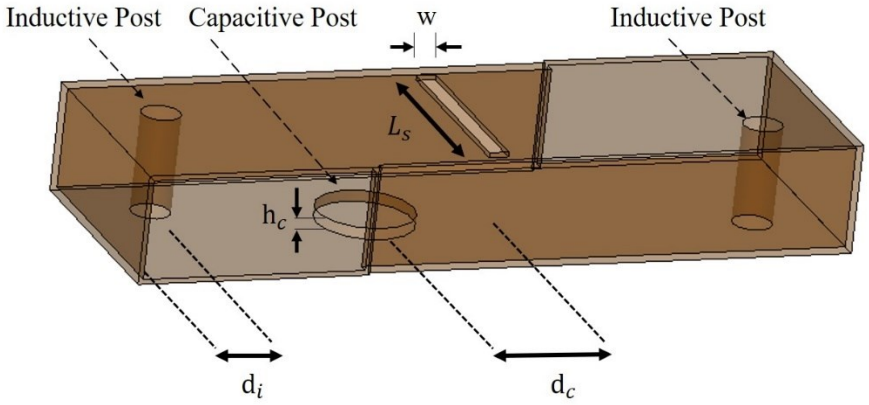

Figure 4. 2 Unit cell of the proposed frequency scanning antenna with introduction of capacitive and inductive posts for open stopband suppression

The distance of the inductive post from the walls, d_i and its radius r_i determine the inductive value of this post, and the height h_c, and the radius r_c of the capacitive post specify the capacitive value of the post. The distance between center of the capacitive post and center of the slot antenna, d_c, helps in impedance matching like moving along a constant susceptance curve in the Smith Chart. The effect of inductive and capacitive posts in impedance matching of two bends in a

unit cell is compared in Figure 4.3 (a) for the unit cell with the slot antenna designed at center frequency of 9.6 GHz with the dimensions provided in Table 4.1.

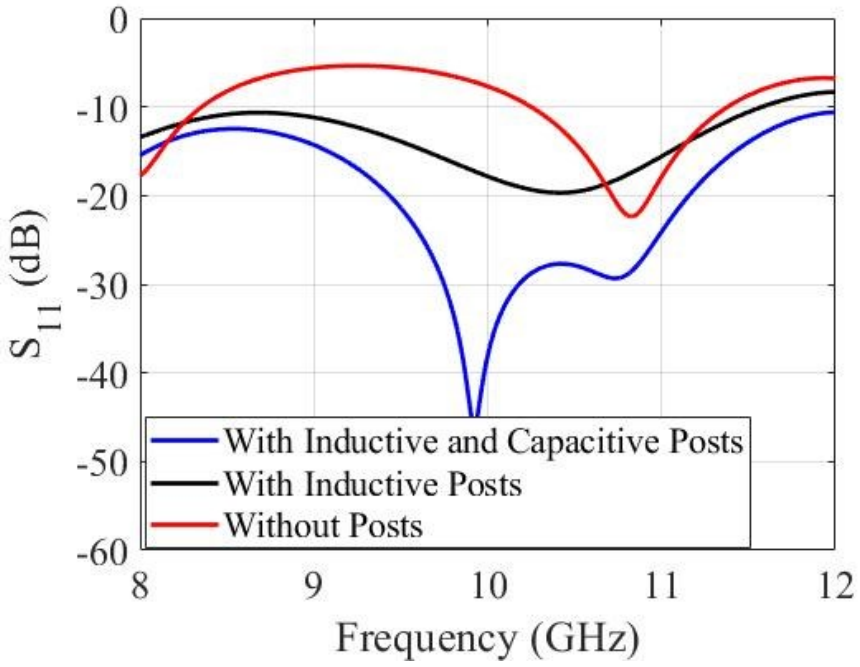

Figure 4.3 Effect of the inductive and capacitive posts on the reflection coefficient of the unit cell when the second port is matched.

Table 4. 1 Dimensions of the Frequency Scanning Antenna Unit Cell (unit: mm)

d_i	r_i	d_c	r_c	h_c	L_s	w
3.4	26.5	10.5	2	1.5	4.8	8

It is observed that the unit cell is well matched when the posts are present, and the second port is matched. Since the effect of the open-stopband starts to be appear when number of elements increases, this effect and how it is suppressed is shown for a 10-element antenna array in Figure 4.4. The comparison is among when there is no post, there are only inductive posts at the bends, and there are all of the designed posts. It is observed from Figure 4.4 that the open-stopband is completely suppressed.

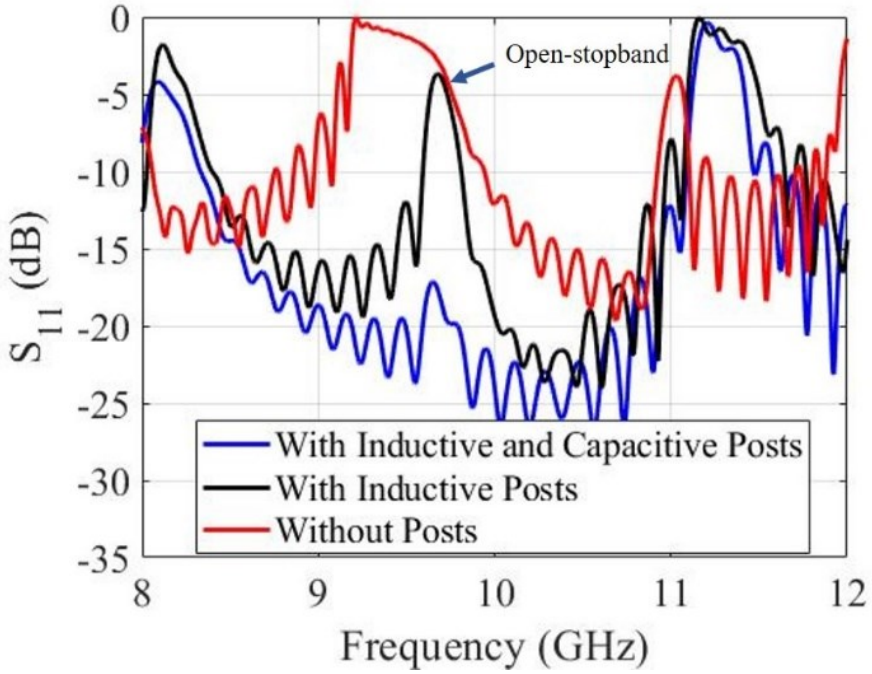

Figure 4.4 Effect of the inductive and capacitive posts on suppression of the open-stopband in the 10-element slot antenna array when the second port is matched.

The simulated radiation patterns of the frequency scanning antenna at 9, 9.6, 10, 10.5 GHz are plotted in Figure 4.5. It is observed that the antenna has its highest gain at around center frequency, and no open-stopband is observed in the antenna realized gain. The antenna main beam scans from -15◦ to 15◦ while the frequency is scanned from 9 to 10.5 GHz. As the frequency goes higher than 10.5 GHz, the next space harmonic of the leaky-wave mode starts propagating resulting in a growing sidelobe.

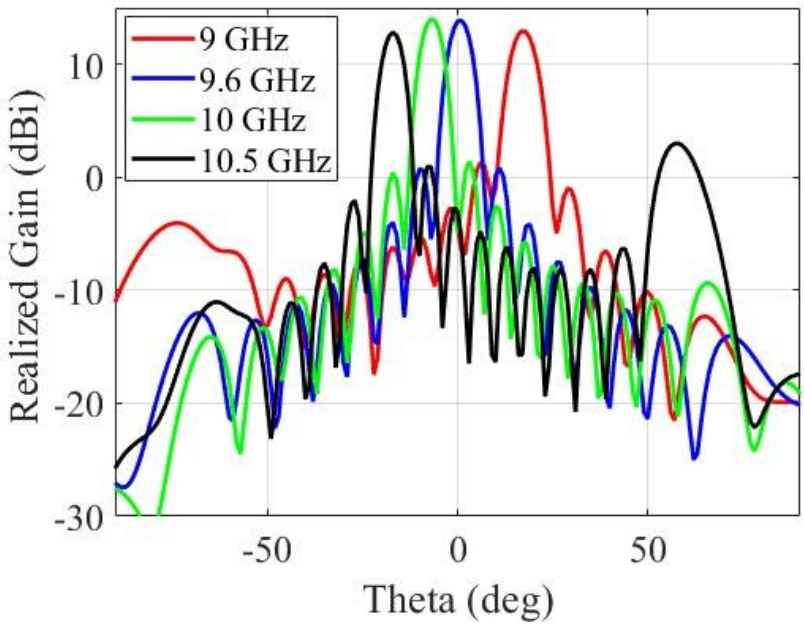

Figure 4. 5 Radiation patterns of the frequency scanning antenna at 9, 9.6, 10, and 10.5 GHz.

The antenna was fabricated using 3-D printing and conductive coating using the metal painted plastic method discussed in the Chapter 2. First, the antenna structure was split into two halves. Then, using an Ultimaker S5, the

antenna was 3-D printed in PLA with 0.09 mm vertical resolution. Finally, the antenna was conductive coated by airbrushing Caswell conductive paint to the surfaces of the antenna. The antenna S_{11} and S_{21} are measured and compared with the simulation in Figure 4.6. The results show that the 3-D printed FSA covers from 8.16 to 11 GHz, while the open stopband is well suppressed. And the E-plane radiation pattern of the antenna over the bandwidth is measured and plotted in Figure 4.7. It agrees with the simulation while showing a beam-scanning with the frequency sweep.

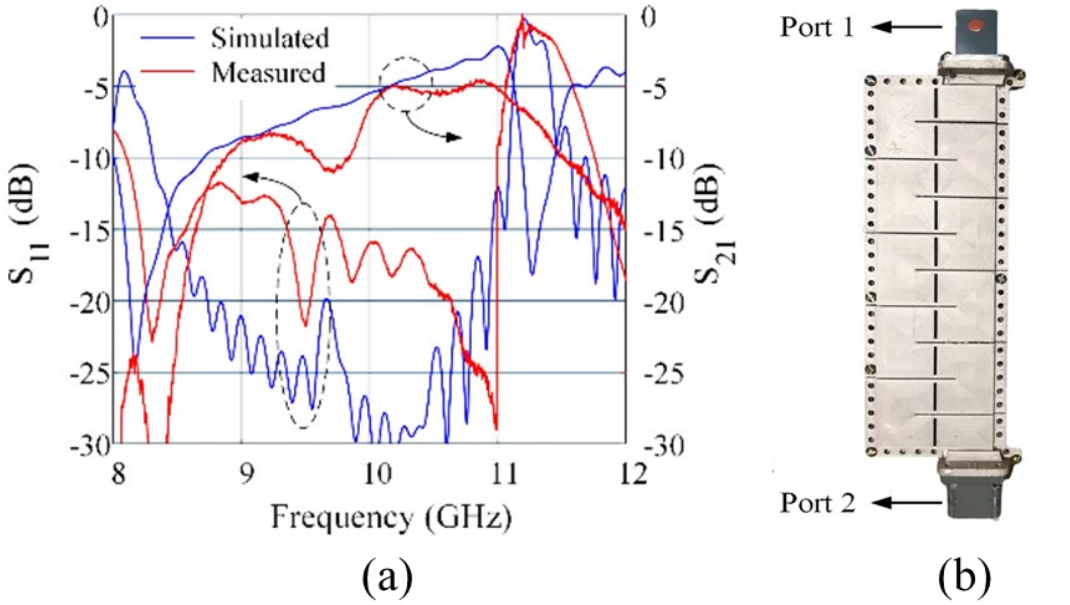

Figure 4.6 (a) Comparison of simulated and measured scattering parameters of the frequency scanning antenna when port 2 is matched, (b) fabricated frequency scanning antenna.

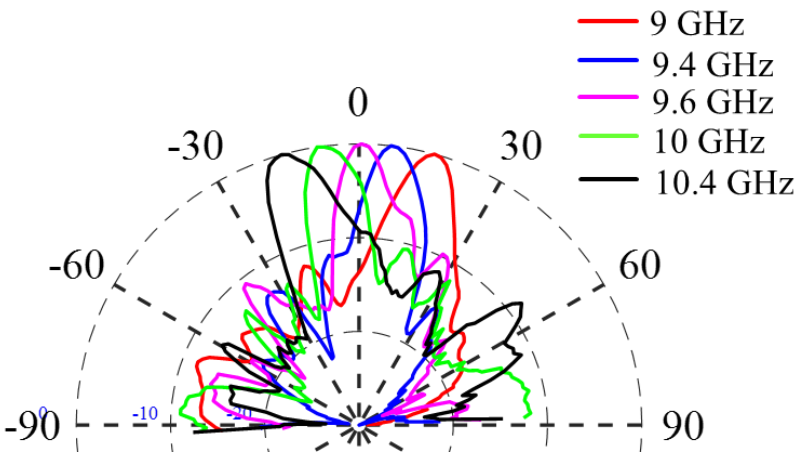

Figure 4. 7 Measured radiation pattern of the frequency scanning antenna at 9, 9.4, 9.6, 10, and 10.4 GHz.

4.3 Design of a 3D-printed High-Directivity H-plane Horn Antenna with High Front-to-back Ratio Using Soft and Hard Walls

Based on the literature [58], the optimum directivity for an H-plane horn antenna can be achieved when $W=\sqrt{3\lambda L}$, where λ is the wavelength, W is width of the horn and L is the distance between the focal point and the horn aperture according to Figure 4.8 (a). Based on aperture antenna theory, the maximum directivity corresponds to a uniform field distribution on the aperture [58]. The closer to uniform aperture distribution the higher the directivity

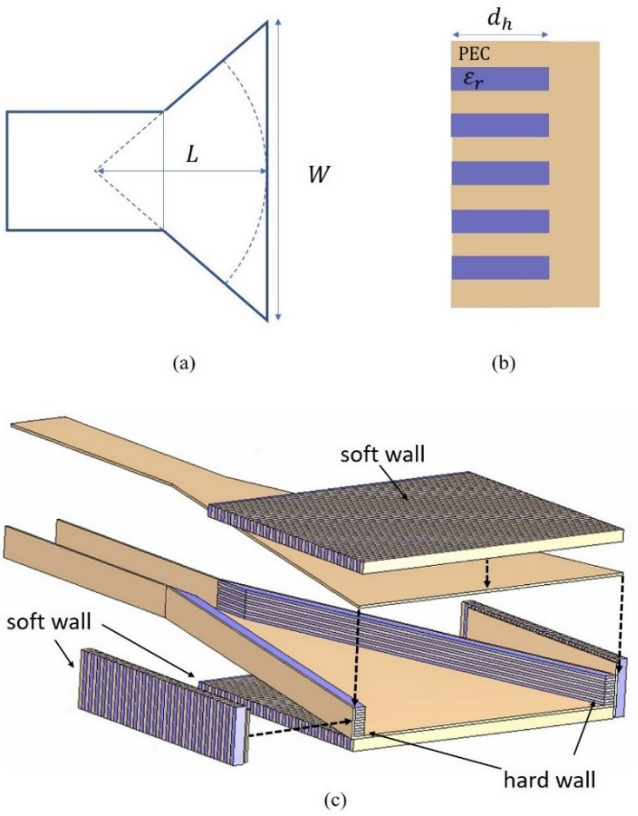

Figure 4. 8 (a) Structure of an H-plane horn antenna from top, (b) corrugated wall filled with dielectric, (c) and the antenna with soft and hard walls (the top walls are exploded to show detail).

As a result, to improve the directivity one solution is employing hard walls inside the horn flares to prepare a uniform amplitude distribution on the aperture. A hard wall refers to a transverse wall that has high reactance, so the field intensity at the wall is high, resulting in uniform aperture distribution [59]. A hard wall can be artificially realized by corrugating a wall in the longitudinal direction and filling the corrugations with dielectric material with permittivity ε_r [60]. The corrugation depth should be:

$$d_h = \lambda/4\sqrt{\varepsilon_r - 1} \qquad (4.1)$$

and width of the corrugations needs to be much smaller than $\lambda/2\sqrt{\varepsilon_r}$ [59]. In addition to improving the directivity, using soft walls can suppress back-radiation from the antenna improving the radiation efficiency and the front-to-back ratio. A soft wall has a small value of transverse wall reactance, so the field is ideally short-circuited there. Soft walls can be realized with corrugations in the longitudinal direction of propagation, with corrugated walls perpendicular to this direction. Short-circuiting backward radiations using soft walls results in high front-to-back ratio. As a result, in this work, soft walls are utilized on the top and bottom of the aperture.

Here, X-band and 10 GHz are chosen as the frequency band and the center frequency, respectively. The waveguide is 22.86 mm wide and 10.5 mm high. Starting with the basic parameters of the antenna, we set L=210 mm, so W=137.4 mm for λ=30 mm. The horn structure needs to be metalized from the outside because of the considerations for the hard and soft walls. In this design, the goal is to take advantage of PLA, a widely-used material in FDM 3D-printing with ε_r=2.7 and tanδ=0.008, as the dielectric material filling the corrugations (Figure 4.8 (b)). To do so, some modifications need to be done in the design for 3D-printability and ability to conductive coating of the required surfaces. The dielectric fillings of hard walls should be connected with a 1 mm thick dielectric

layer from the top. As a result, by conductive coating the outer side hard walls can be realized. But the corrugation height and the horn width need to be optimized as the dielectric layer is added. For the soft walls, the walls are offset by 5 mm from the horn aperture and the dielectric inserts are connected using a dielectric layer, same as hard walls. Conductive coating the corrugations results in the realization of the soft walls as well. To design the hard and soft walls, the corrugation depth (d_h) is calculated using (1), then optimized. The corrugation depth is 4.8 mm and 3.75 mm for the hard and soft walls, respectively. The width of the corrugations is 1.5 mm. As shown in Figure 4.8 (c), hard walls are arranged inside the horn flare transversely, and soft walls are located outside of the horn.

The antenna is 3D-printed in PLA using FDM 3Dprinting method, and then the required surfaces are conductive coated using airbrushing copper paint as shown in Figure 4.9.

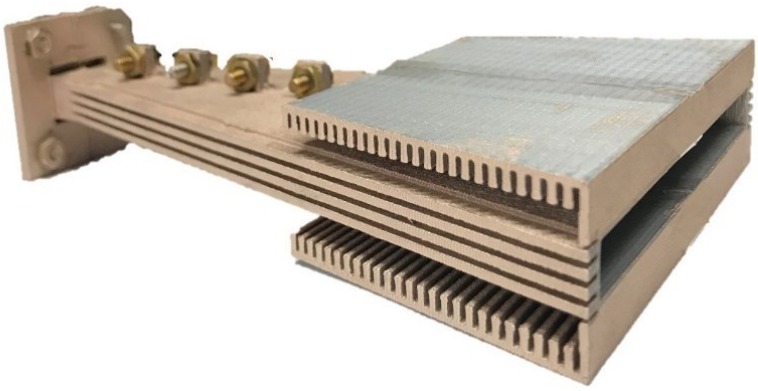

Figure 4.9 3D-printed and conductive coated H-plane horn antenna with high directivity and suppressed back radiation.

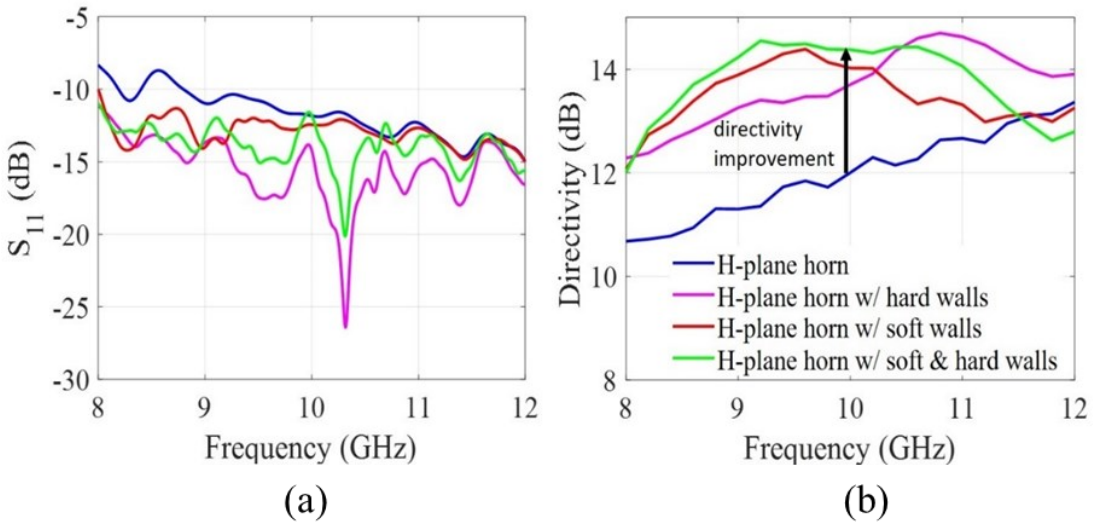

Figure 4.10 Comparison of an H-plane horn antenna having hard walls, soft walls, and with both hard and soft walls. (a) S_{11}, (b) directivity.

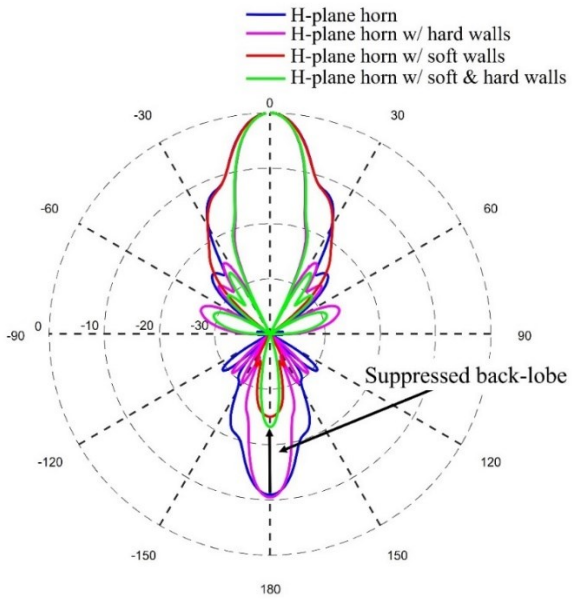

Figure 4. 11 Normalized H-plane radiation pattern comparison.

The antenna designed based on the discussed considerations is simulated using CST Studio Suite. Comparison of the H-plane horn antenna without soft

and hard walls to one having only hard walls, one having only soft walls, and one with soft and hard walls is done in Figures 4.10 and 4.11. The antenna return loss is compared in Figure 4.10 (a). Although the basic H-plane horn lacks good return loss over the band, the design with soft and hard walls does show good return loss over X-band. As shown in Figure 4.10 (b), antenna directivity is improved over the band as well. At 10 GHz, directivity is enhanced by 2.4 dB from 12 dB to 14.4 dB by adding hard and soft walls; using only hard walls it improves by just 1.5 dB. The H-plane horn antenna has a fan-beam at the E-plane and a narrow beam at its H-plane. Here, H-plane radiation is of primary concern. So, H-plane radiation patterns of the antennas are compared in Figure 4.11. Hard walls give directive radiation patterns and soft walls suppress backward radiation.

In addition, the radiation pattern of the antenna using both hard and soft walls benefit from both having high directivity and low backward radiation, the front-to-back ratio is improved by 13.7 dB. Finally, the fabricated antenna is measured, and the results are compared with simulations in Figure 4.12.

A good agreement in comparison of H-plane radiation patterns at 10 GHz are shown in Figure 4.12. The gain plots in Figure 4.13 show a comparable gain measurement while some losses are because of using copper paint as its conductivity is less than bulk copper. And the reflection coefficient shows a good

agreement between simulation and measurement for the antenna covering the X-band.

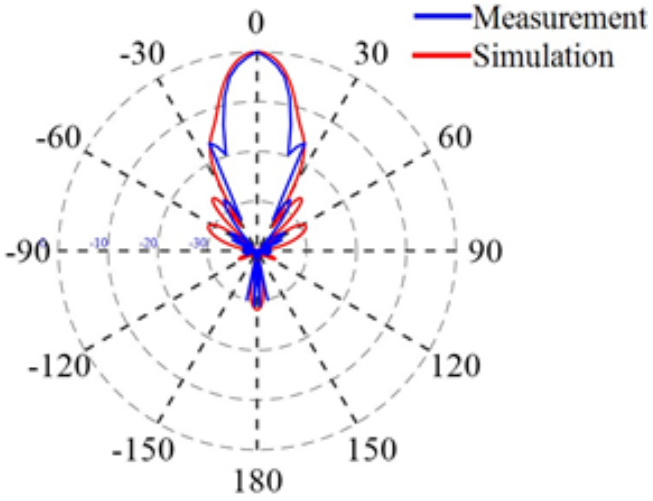

Figure 4.12 Radiation patterns comparison of measurement with simulation

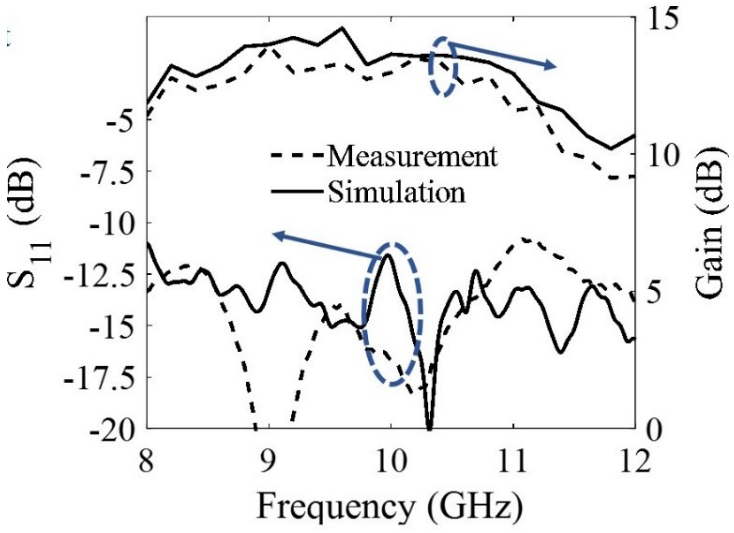

Figure 4.13 Return loss and antenna gain comparison of measurement with simulation.

4.4 Conclusion

In this Chapter, first, a slot array frequency scanning antenna fed via a meandered rectangular waveguide was designed and 3-D printed. To match the waveguide bends, and to suppress the open-stopband, inductive and capacitive posts were designed to be located inside the rectangular waveguide at certain locations. The simulation and measurement results prove that the bends are well matched, the open stopband is completely suppressed, and the antenna has a bandwidth from 8.16 to 11 GHz in practice. The designed antenna scans 30^o symmetrically around broadside while scanning the frequency from 9 to 10.5 GHz.

Then, an H-plane horn antenna with hard and soft walls was designed to benefit from 3D printing capabilities. As a result, it can be fabricated easily, without the drawbacks of SIW technology. Using hard and soft walls directivity and front-to back ratio are enhanced by 2.4 dB, and 13.7 dB, respectively, compared to a standard H-plane horn antenna, while the bandwidth covers X-band with lower return loss. The measurement results of the 3D-printed and conductive coated antenna show a wide bandwidth covering X-band and radiation patterns and antenna gain are in good agreement with the simulation.

5 An Integrated Probe for Near-field Antenna Measurement

5.1 Introduction

Over-the-Air measurement systems are of interest for modern electronic systems devices that are highly integrated [61].For instance, current and future mobile-device antennas are packaged and surrounded by circuits, rendering impractical conventional methods of antenna measurement that use bulky connectors. Furthermore, moving toward the 5G millimeter-wave spectrum, far-field measurements need a large chamber if the device under test is large compared to the wavelength, e.g. a small-cell base station (Table 5.1).

Table 5. 1 Far-field distance (meter) for antennas with different dimensions

D(mm)	28 GHz	39 GHz	60 GHz
50	0.47	0.65	1
100	1.9	2.6	4
150	4.2	5.9	9
200	7.5	10.4	16
300	16.8	23.4	36

At mm-wave frequencies, the path loss also limits far-field test setups as it corresponds to frequency squared as well as distance squared. On the other hand, conventional near-field measurement setups are expensive since they consist of high-performance instruments. In addition, test and verification of the electronic

products must be fast in production. Therefore, there is a demand for a method to measure near-field radiation of the antenna with low loss, quickly and at low cost.

Near-field antenna measurement is usually done in different coordinates and using different probe types. In [62], a wideband probe is designed based on an exponentially tapered ridge in the rectangular waveguide. In [63], an optically modulated scatterer is designed to be used as an electric-field probe. In addition, open-ended waveguide is widely used as an electric-field probe in different nearfield measurement setups [64], [65]. None of these solutions can simplify the near-field measurement and data acquisition setup. Furthermore, they do not have the capability of being expanded to a probe array to speed up near-field scan because they are bulky.

(a) (b)

Figure 5.1 Examples of antenna measurement systems: (a) Planar near-field scanner by NSI-MI [66] (b) A compact antenna test range [66]

In this section, we propose a high-performance, compact, and low-cost probe for near-field antenna measurement. By down-converting the near-field signal at the probe location, the output signal can be analyzed with a simple setup rather than a high frequency spectrum analyzer. This probe can be expanded to an array of probes, shown in Figure 5.2, using the same feed for making the near-field antenna measurement fast.

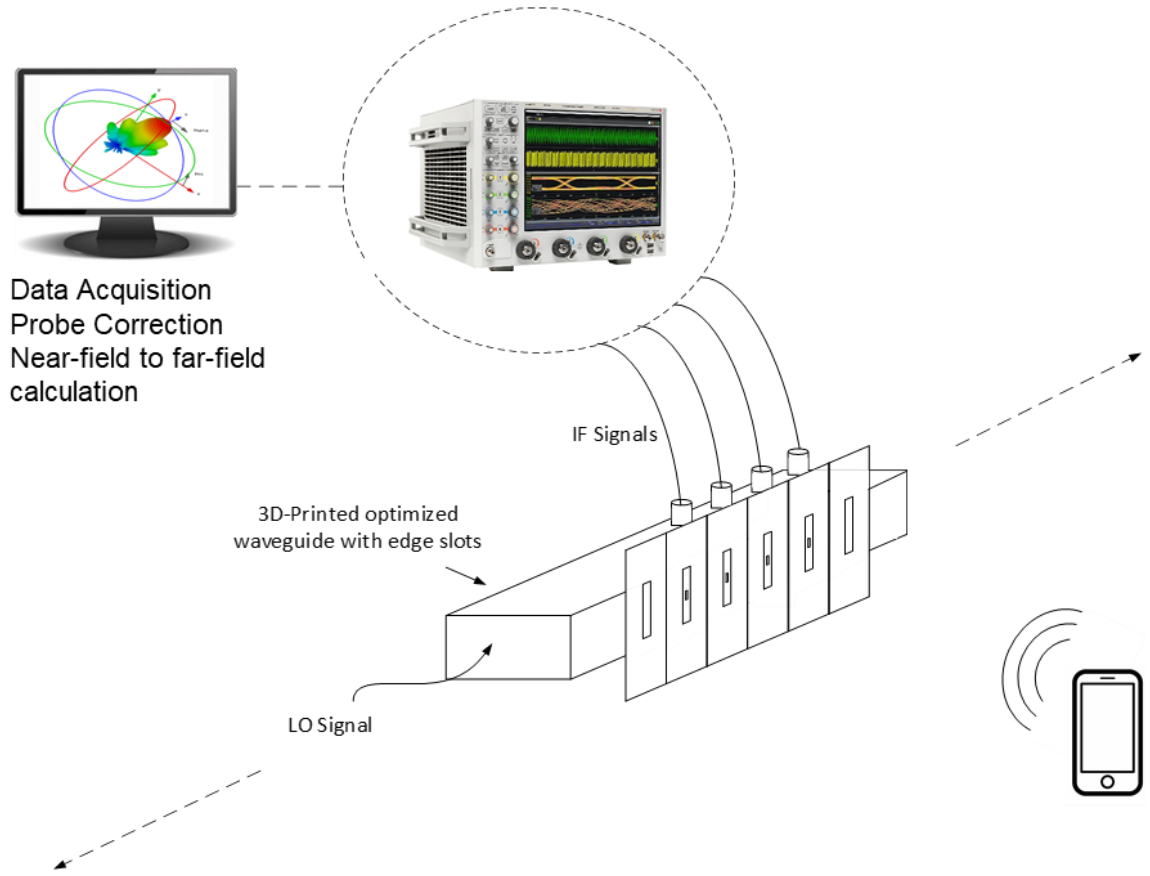

Figure 5.2 Array of single polarized probe proposed for near-field antenna measurement.

5.2 Probe Design, Simulation, and Fabrication

For high performance, the RF signal should be down-converted as close as possible to the probe. To do so, the mixer should be placed at the probe and the LO should illuminate the mixer as well. To simplify the system, a diode quad mixer is used, which is self-biased, requiring neither bias lines nor a separate power supply. The LO is transferred to the mixer through waveguide transmission. We take the unbalanced IF signal out from the transformer on the RF or LO side as shown in Figure 5.3.

The requirements above suggest a probe design of three layers. On the top layer, there is a slot antenna for near-field signal measurement, on the bottom layer, a 45-degree oriented slot for coupling the LO from a slot cut on a sidewall of the waveguide, and the middle layer, ground plane for the top slot, which also isolates RF to LO leakage and vice versa. There are two plated via holes attached to the middle of the 45-degree-oriented slot to transfer the LO to the top plane. Using 45-degree oriented gives the highest coupling of LO to the two plated via holes. The probe configuration is shown in Figure 5.3. Narrow slits cut through the slot enable the IF signal to be routed to the edges of the slot. In practice, the slit cut transforms the balanced signal to an unbalanced one since slot antennas are inherently balanced. Two capacitors connect the separated regions of the slot to avoid decreasing the RF performance of the slot yet provide high impedance

at IF. To avoid the influence of a bulky connector on the RF signal, the IF output connector is located on the back.

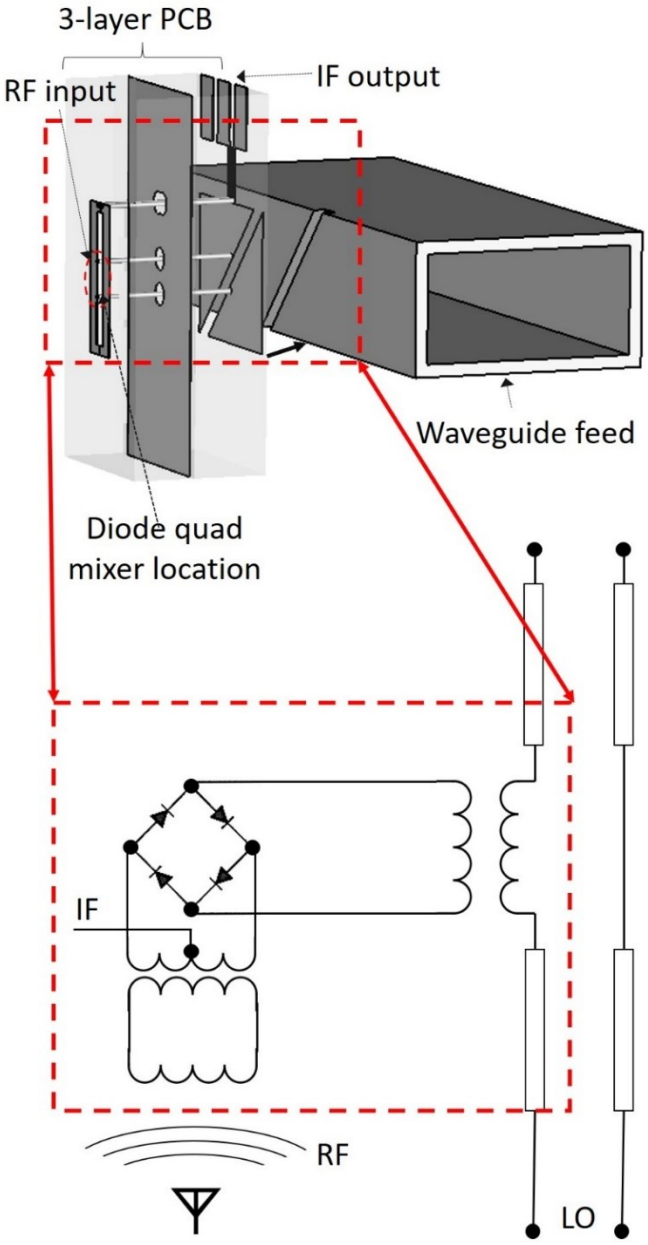

Figure 5.3 Probe design and its schematic including a diode quad mixer, a transmission line, and couplers.

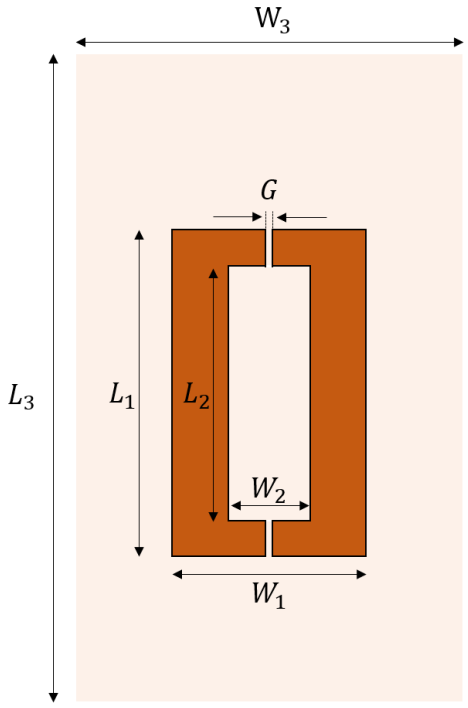

Figure 5.4 Slot probe dimensions

The primary portion of the probe is the front slot. Here, the capacitive loading effect of the diode quad mixer has been considered in the slot probe design resulting in a probe that covers bandwidth of 0.5 GHz around 10 GHz. Detailed parameters of the slot are in Figure 5.4. and values are $\mathrm{L}_1 = 12\ mm$, $\mathrm{L}_2 = 7.8\ mm$, $\mathrm{L}_3 = 30\ mm$, $\mathrm{W}_1 = 4\ mm$, $\mathrm{W}_2 = 1.1\ mm$, $\mathrm{W}_3 = 15\ mm$ and $\mathrm{G} = 0.1\ mm$. The probe is fabricated on FR4 substrate, 2.4 mm for the front slot and 2 mm thick for the back slot. The front slot antenna has 7 dBi directivity, and 0 dBi gain in far-field with 63^o half-power beamwidth (HPBW) in the H-plane. The far-field E-plane and H-plane radiation patterns of the probe

are shown in Figure 5.5. The effect of the non-ideal probe can be removed from the near-field data using a probe correction method [67].

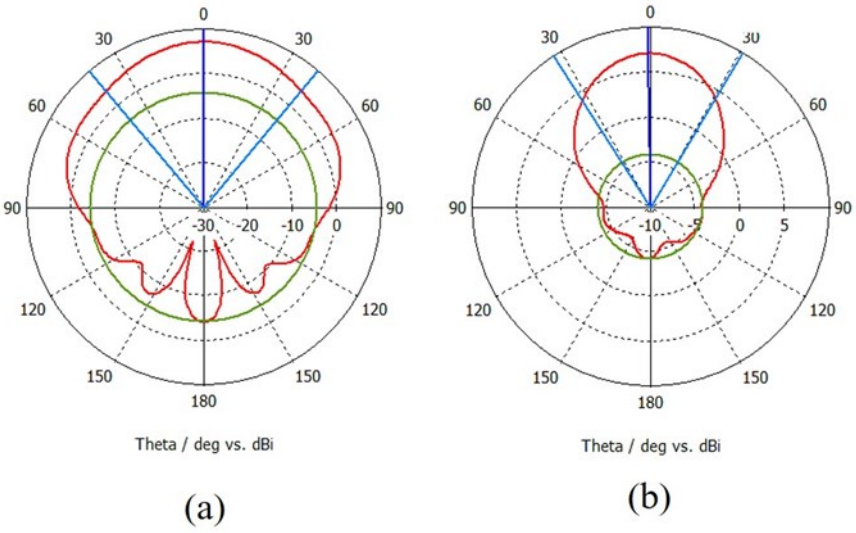

Figure 5.5 Simulated (a) E-plane and (b) H-plane far-field radiation patterns of the probe.

The back slot, which gets the LO from the waveguide and transfers it to the front side, is 45-degree oriented with a width of 1.3 mm and length of 16 mm. The same dimensions of cutout in the waveguide sidewall matches the 45-degree-oriented slot on the PCB and couples the LO to it. Through two plated via holes, which pass through the middle layer, the LO drives two pads on the front slot plane where the LO port of the mixer is. Therefore, the mixer can be soldered on the front plane, mixes RF with LO, and produces output (IF) which can be taken out from the slit cut. The waveguide feed is a standard WR-90 waveguide which

enables multiple probes arranged side-by-side, reducing antenna near-field measurement scan time significantly.

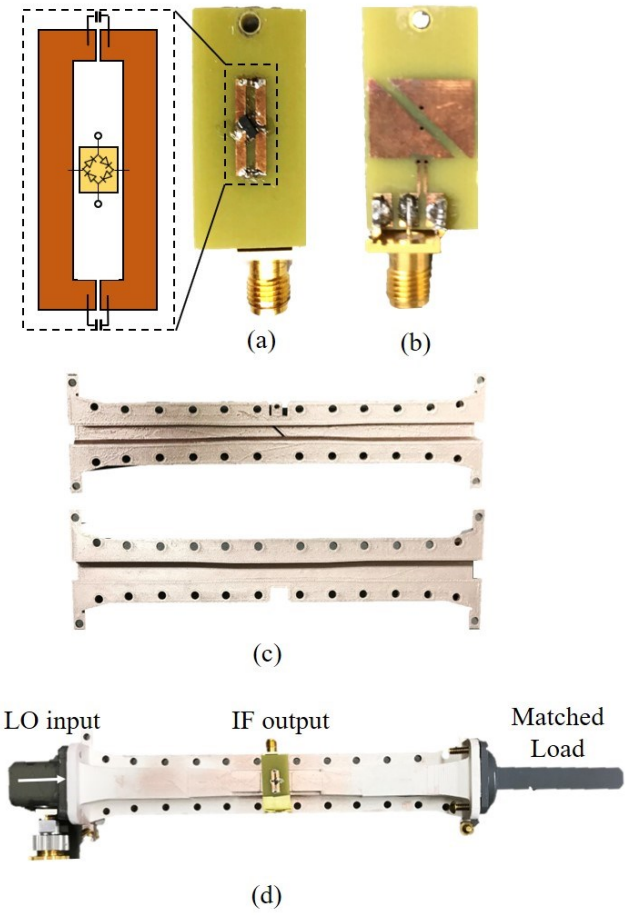

Figure 5.6 Probe parts: (a) PCB top view, slot antenna including a mixer, (b) PCB bottom view, 45-degree-oriented slot, and the output, (c) 3D-printed and copper coated waveguide halves, and (d) complete probe setup including a matched load connected to the end of the waveguide.

The diode quad mixer (Avago HSMS-2829) is soldered on the probe plane shown in the inset of Figure 5.6 (a). The LO feed is a rectangular waveguide, 3D printed in plastic and prepared using a plastic conductive coating method. 3D

printing makes it easy to realize a fine slot cut in one of the walls. The complete probe setup is shown in Figure 5.6 (d). Using HSMS-2829 for the LO power ≥10 dBm, the IF frequency does not affect the IF power. Figure 5.7 shows IF at LO = 10 dBm compared with LO = 0 dBm. Sufficient LO power (10 dBm) (e.g. at 10 GHz) guarantees the same output power at different IF and avoids the need for power calibration at each IF.

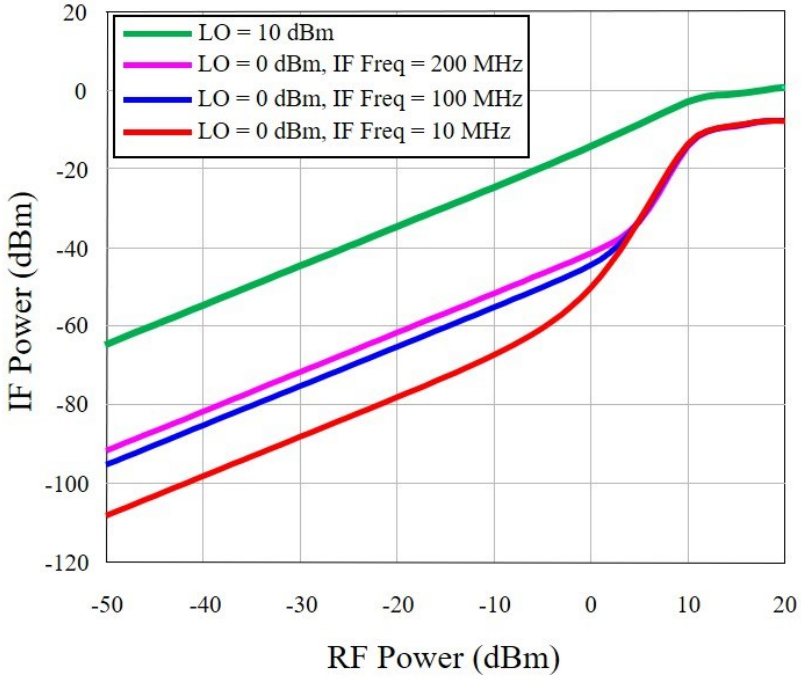

Figure 5.7 IF (output) power for LO power = 0 dBm, and LO power = 10 dBm for different IF frequencies. At LO power = 10 dBm, the IF power is independent of IF Probe Characterization

To evaluate the probe performance in a practical scenario, the transfer response is measured at fixed distance of 10 cm for the X-band standard horn

antenna (FXR X638A) used in this project. To do so, the IF frequency is fixed at 10 MHz, RF power fixed at 17 dBm, and LO and RF frequencies are swept over the X-band while keeping the Δf=10 MHz. The IF power captured by the mixer vs. LO frequency is plotted in Figure 5.8. The center frequency of the probe is shifted down to 9.5 GHz. It can be because of dielectric properties variation of the probe substrate, or different loading capacitance value of the diodes (C_{J0} = 0.7 pF) compared to the datasheet [].

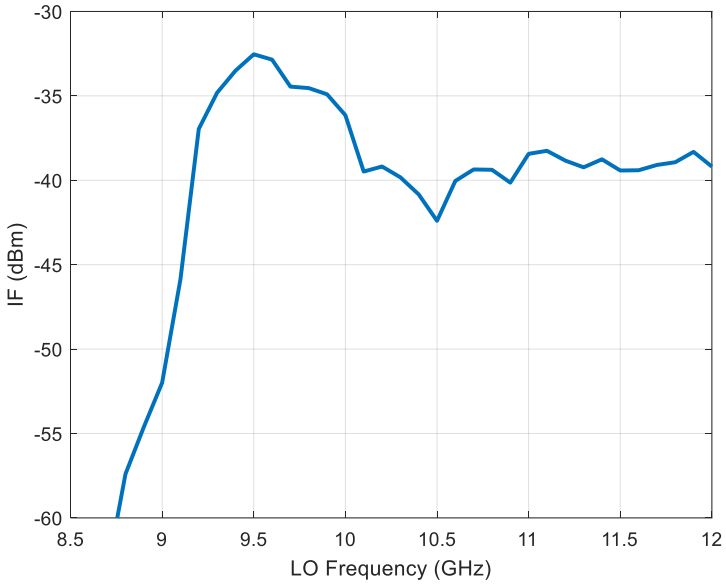

Figure 5.8 IF power (dBm) vs. LO frequency sweep for the fixed RF power = 17 dBm and the distance to the AUT of 10 cm.

To improve the performance of the probe an iris-coupled filter is designed and added to the waveguide that carries LO. The waveguide including the iris-coupled filter is fabricated with the 3D-printing and copper coating method

discussed previously and shown in Figure 5.9. This will improve LO coupling to the slot, then to the mixer, resulting in improving the dynamic range in the bandwidth of the probe.

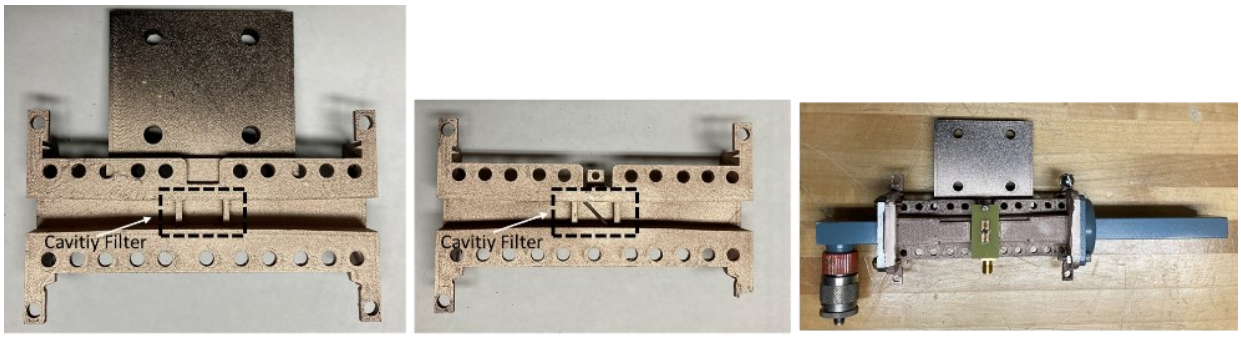

Figure 5.9 Waveguide with iris-coupled cavity filter for improvement of LO coupling to the 45-degree oriented slot. (a) bottom of the waveguide, (b) top of the waveguide, and (c) the new probe setup with the filter added to the waveguide.

Figure 5.10 shows the improvement of received IF compared to the probe mounted on the waveguide with no cavity filter. At 9.5 GHz, 5 dB improvement is measured with adding the iris-coupled filter to the setup.

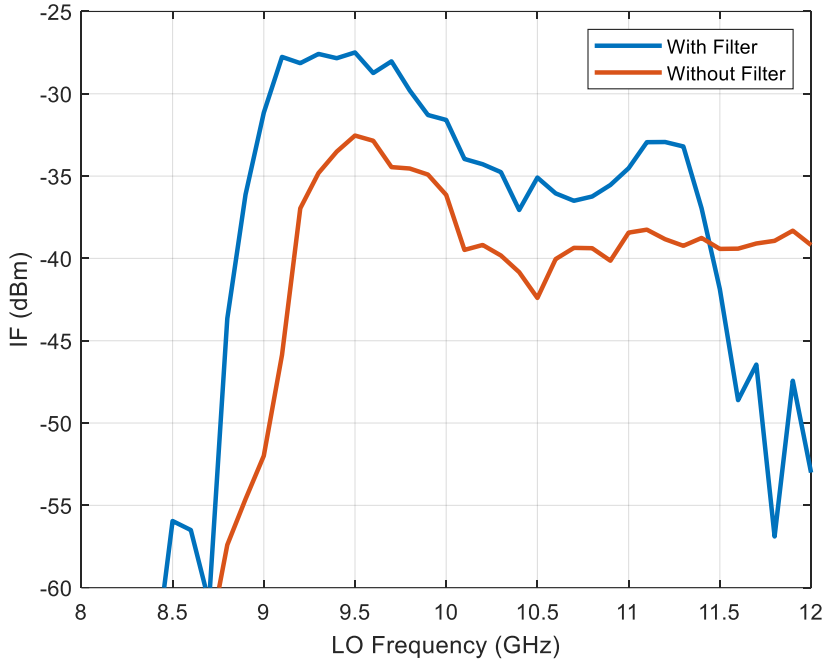

Figure 5.10 Comparison of IF power response vs. LO frequency for the waveguide with and without iris-coupled filter.

Now that the performance of the probe is improved, a sensitivity test needs to be done. The goal of this test is to find the relation of IF power vs. RF power when sweeping RF power, and fixing LO power = 35 dBm, LO frequency = 9.5 GHz, and distance to the AUT of 10 cm. The result of the sensitivity test is plotted in Figure 5.11. The linear response shows that the probe response has a one-to-one relation with the RF power from AUT and it is away from the saturation region of the probe. Since the measurement bandwidth is 10 MHz, this system can work properly until RF power = -35 dBm without getting close to the noise floor. It means that this probe can easily cover at least 45 dB of dynamic range which is suitable in near-field analysis such as an over-the-air antenna

measurement [9] Near-field antenna measurement using this probe requires calibration for actual near-field data. The measured IF power should be transformed to the corresponding actual RF power using the IF power vs. RF power relationship (Figure 5.11). Since it is a monotonic function, there is no ambiguity in finding the corresponding RF power. Using the same method phase response is measured at IF and can be used in the nearfield to far-field calculation.

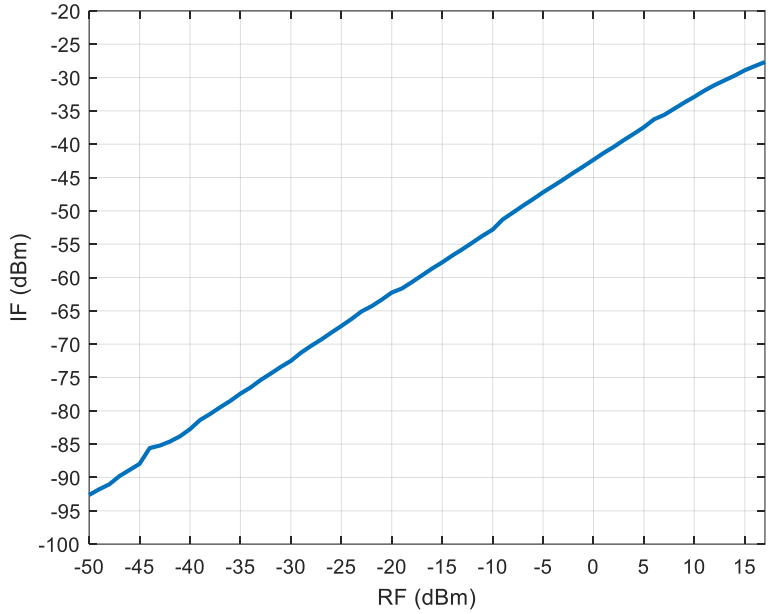

Figure 5.11 Probe sensitivity test: IF (dBm) vs. RF (dBm), while fixing LO power = 35 dBm, LO frequency = 9.5 GHz

In the next chapter, as the continuation of this chapter, the near-field to far-field technique, near-field measurement using the proposed probe, and probe correction are discussed.

6 Low-cost Near-field Antenna Measurement Setup

6.1 Introduction

Antenna characterization is the inevitable task in any antenna design procedure. Antenna engineers require to know how the antenna radiates, and what the gain and radiation efficiency are in practice in addition to reflection coefficient and couplings to make sure the antenna is working in the specific scenario. Comparison of the measured results with simulations needs to be in a good agreement to make the antenna engineer confident about the model. However, in some practical scenarios, making a complete model is not feasible due to the complexity of the surrounding environment. Therefore, an accurate measurement setup is essential for antenna design problems.

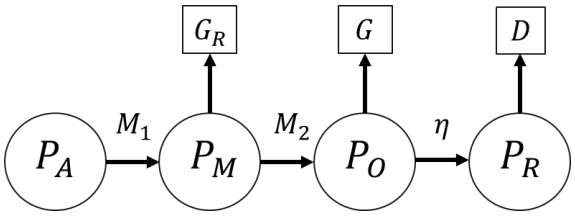

Figure 6. 1 Power flow from source to an antenna. Realized gain (G_R), gain (G), and Directivity can be measured based on delivered power (P_M), to the antenna accepted power (P_O) by the antenna and radiated (P_R).

From measured S-parameters, return loss or mismatches (M_1 , M_2), and accepted power (P_O) by the antenna can be studied. Then, how much of the accepted power is radiated (P_R) and how the antenna radiates in far-field

(Directivity) can be studied by radiated measurement. Figure 6.1 shows a summary of different input powers, antenna gain and directivity, and efficiency definitions.

Antennas are mainly designed based on their far-field radiation because of their applications in communication. Therefore, the characterization needs to be done in far-field region. But, at higher frequencies the required distance to satisfy far-field condition becomes larger which makes the setup impractical. It is where alternative solutions such as near-field measurement, and Compact Antenna Test Range (CATR) become reasonable solutions. In every near-field measurement setup, there is a need for a Network Analyzer or a pair of signal generator and signal analyzer to capture the relative amplitude and phase. Such instruments become expensive at high frequencies, such as millimeter-wave (mm-wave), and make the setup costly.

In this Section, a near-field antenna measurement setup is built based on the single probe discussed in the previous chapter. The main idea is to down-convert the RF signal to a low-frequency signal which can be measured with a simple instrument. Using the near-field data, far-field radiation pattern is calculated and then the effect of the probe is corrected.

6.2 Near-field to far-field transformation in planar system

The technique of near-field to far-field transformation is driven from the surface equivalence theorem and Huygens' Principle. Based on them, by knowing the surface currents on any shape surrounding the electric field source the radiation can be calculated at any other surfaces. By expansion of this to far-field, we can calculate far-field by knowing near-field radiation of an antenna.

The near-field measured data, which is amplitude and phase of the electric or magnetic field, are measured by a scanning field probe over a surface which may be a plane, a cylinder, or a sphere. The measured data are then transformed to the far-field using analytical Fourier transform methods. Among three coordinate systems for near-field measurement, planar one is the simplest in building the setup and requires less complex analytical calculation. In general, the planar system is suitable for high-gain antennas, and it requires the least number of computations and no movement of the antenna. The spherical system requires more computation, and more expensive positioning setup. This system is best suited for measurements of low-gain and omnidirectional antennas. The cylindrical system is the compromise between planar and spherical system [58].

The fundamental formulations of the planar near-field to far-field system is based on the plane wave (modal) expansion using Fourier transform (spectral)

techniques. In electromagnetics, based on plane wave expansion, any monochromatic wave can be decomposed to superposition of plane waves traveling in different directions, with different amplitudes, but all the same frequency. The purpose of the plane wave expansion is to determine the unknown amplitudes and directions of propagation of the plane waves [58].

The relationships between the near-field and the far-field for a planar system can be appreciated through transform (spectral) techniques:

$$\mathbf{E}_{(x,y,z)} = \frac{1}{4\pi^2}\int_{-\infty}^{\infty}\int_{-\infty}^{\infty}\mathbf{f}(k_x,k_y)e^{-j\mathbf{k}.\mathbf{r}}dk_x dk_y \quad (6.1)$$

where

$$\mathbf{f}(k_x,k_y) = \hat{a}_x f_x(k_x,k_y) + \hat{a}_y f_y(k_x,k_y) + \hat{a}_z f_z(k_x,k_y) \quad (6.2)$$

$$\mathbf{k} = \hat{a}_x k_x + \hat{a}_y k_y + \hat{a}_z k_z$$

$$= \hat{a}_x x + \hat{a}_y y + \hat{a}_z z$$

where $\mathbf{f}(k_x,k_y)$ represents the plane wave spectrum of the field. The x and y components of the electric field measured over a plane surface (z = 0) from

$$\mathbf{E}_{xa(x,y,z=0)} = \frac{1}{4\pi^2}\int_{-\infty}^{\infty}\int_{-\infty}^{\infty} f_x(k_x,k_y)e^{-j(k_x x+k_y y)}dk_x dk_y \quad (6.3)$$

$$\mathbf{E}_{ya(x,y,z=0)} = \frac{1}{4\pi^2}\int_{-\infty}^{\infty}\int_{-\infty}^{\infty} f_x(k_x,k_y)e^{-j(k_x x+k_y y)}dk_x dk_y \quad (6.4)$$

The x and y components of the plane wave spectrum $f_x(k_x, k_y)$ and $f_y(k_x, k_y)$ are determined in terms of the near-field from the Fourier transforms of (6.3) and (6.4).

$$f_x(k_x, k_y) = \int_{-\frac{b}{2}}^{\frac{b}{2}} \int_{-\frac{a}{2}}^{\frac{a}{2}} \mathbf{E}_{xa(x',y',z'=0)} e^{+j(k_x x' + k_y y')} dx' dy' \quad (6.5)$$

$$f_y(k_x, k_y) = \int_{-\frac{b}{2}}^{\frac{b}{2}} \int_{-\frac{a}{2}}^{\frac{a}{2}} \mathbf{E}_{ya(x',y',z'=0)} e^{+j(k_x x' + k_y y')} dx' dy' \quad (6.6)$$

Then, far-field can be calculated from the plane wave spectrum function **f**:

$$E(r, \theta, \varphi) \simeq j \frac{k e^{-jkr}}{2\pi r} \left[cos\theta \mathbf{f}(k_x, k_y) \right] \quad (6.7)$$

Or to decompose E_θ and E_φ :

$$E_\theta(r, \theta, \varphi) \simeq j \frac{k e^{-jkr}}{2\pi r} \left[f_x cos\varphi + f_y sin\varphi \right] \quad (6.8)$$

$$E_\varphi(r, \theta, \varphi) \simeq j \frac{k e^{-jkr}}{2\pi r} cos\theta \left[-f_x sin\varphi + f_y cos\varphi \right] \quad (6.9)$$

From 6.1 to 6.9, the far-field radiation pattern can be determined by the near-field measurement. First, $\mathbf{E}_{xa}$ and $\mathbf{E}_{ya}$ are needed to be measured at distance z=z_0 from the antenna aperture on a planar surface. z_0 should be at least two or three wavelengths to be out of the reactive near-field region. The simplest plane over which measurements can be done is made of dividing the plane into a

rectangular grid of M × N points spaced Δx and Δy apart [58]. The measurement area can be trimmed where the signal at the edges of the plane is about 45 dB below the largest signal level within the measuring plane. After defining the scan area, we can divide it to sampling points. To do so, we should consider Nyquist sampling criterion. Therefore, the sampling rate should be less than $\lambda/2$ [58]. Next step is to discretize near-field to far-field transformation formulas.

6.3 Near-field to Far-field Simulations

In planar near-field measurement of an antenna, it is required to sense both horizontal and vertical polarizations of the electric field in the radiative near-field region of the antenna under test (AUT). The sampling steps should be smaller than half of the wavelength so that the far-field radiation can be calculated correctly. The distance between near-field probe and AUT, and the truncation of the scanning range are two important criteria that can limit the accuracy of the far-field calculation. To practice them, a near-field simulation setup is designed in MATLAB, where exact near-field of a Horn antenna is once calculated at different distances and the other time it is calculated for different planar areas. The near-field to far-field calculation is done using the MATLAB program published at [68].

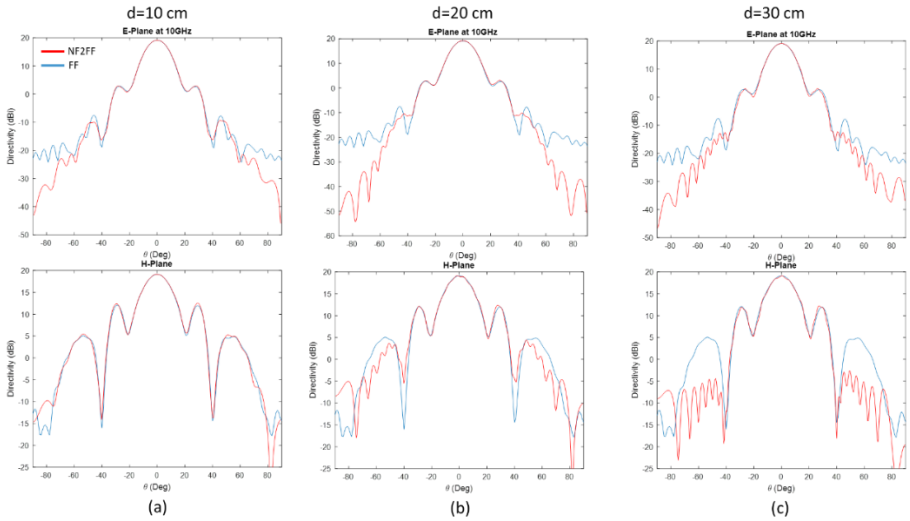

Figure 6. 2 Near-field to far-field calculation of a standard horn antenna simulated in MATLAB. The near-field is captured at 10 GHz at different distances form the antenna aperture: (a) 10 cm, (b) 20 cm, and (c) 30 cm.

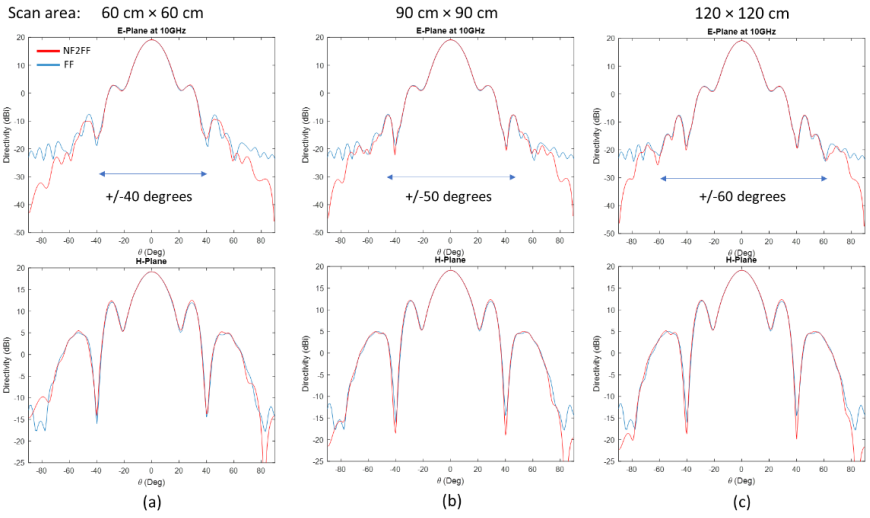

Figure 6. 3 Near-field to far-field calculation of a standard horn antenna simulated in MATLAB. The near-field is captured at 10 GHz at d= 10 cm, with different scan area: (a) 60 × 60 cm, (b) 90 × 90 cm, and (c) 120 × 120 cm.

Figure 6.2 compares how accuracy degrades in near-field to far-field calculation by increasing the distance from the antenna, while the scan area is fixed to 60 × 60 cm. In Figure 6.2 (a), the near-field to far-field calculated E-plane starts getting different from the exact far-field after $\theta = 45$, while H-planes are in good agreement up to $\theta = 75$. But by getting far from the antenna aperture, at d= 20 cm, from $\theta = 35$ calculated E-plane starts getting off from the exact far-field one, and H-plane starts degrading from $\theta = 50$. And, at d= 30 cm, from $\theta = 35$ calculated E-plane starts getting off from the exact far-field one, but H-plane starts degrading from $\theta = 40$. The reason is related to the wave propagation and its expansion by getting far from the antenna aperture. Therefore, by being closer to the antenna aperture the required scan area for a fixed accuracy is smaller. But, in practice, the probe cannot get very close to the antenna because of reflections from probe surface back to the antenna which can change the near-field. In this case, 10 cm is a proper distance while the accuracy of E-plane calculated from near-field compared to the far-field starts degrading from elevation angle of 45 degrees.

The next simulation practice is to find out the effect of scan area on the accuracy range in near-field to far-field transformation. Figure 6. 3 shows the comparison of near-field to far-field calculation with the actual far-field for

different scan area dimensions while the distance to antenna aperture is fixed at 10 cm.

These two practices show that to be able to calculate far-field based on near-field for a wider angle it is better to do the near-field measurement in a closer distance to the AUT, and with wider scanning area. Based on this point, this measurement setup is more suitable for high gain antennas which has focused main beam. For antennas with wide beam, cylindrical and spherical near-field setups are recommended. In this project, we built a planar near-field setup with 60 ×60 cm scanning area. Based on simulations, the distance of 10 cm is fine for the near-field measurement of a standard horn antenna using the designed probe. It means that, due to the small size of the probe, the probe does not perturb near-field radiation of the AUT. Before delving into near-field measurement of an AUT and calculating far-field, it is necessary to study effect of a non-ideal probe on the calculated far-field. In the next section, this topic is discussed and how the effect can be taken out is driven.

6.4 Near-field Measurement Setup

In our near-field measurement setup, LO and RF signals get mixed in the diode quad mixer located on the slot. The diode quad mixer is self-biased and gets enabled by the LO signal power. The IF output is transferred to a Lock-in

Amplifier for measurement of the signal and data acquisition. Then, the data is transferred to a computer, and the far-field radiation pattern is calculated based on the near-field data. Then, the probe radiation pattern is taken out from the far-field to deliver the AUT's far-field radiation pattern. Diagram of the near-field measurement setup is depicted in Figure 6.4. The Lock-in amplifier requires getting sample of the reference signal from the RF signal sources to be able to correctly detect the received signal.

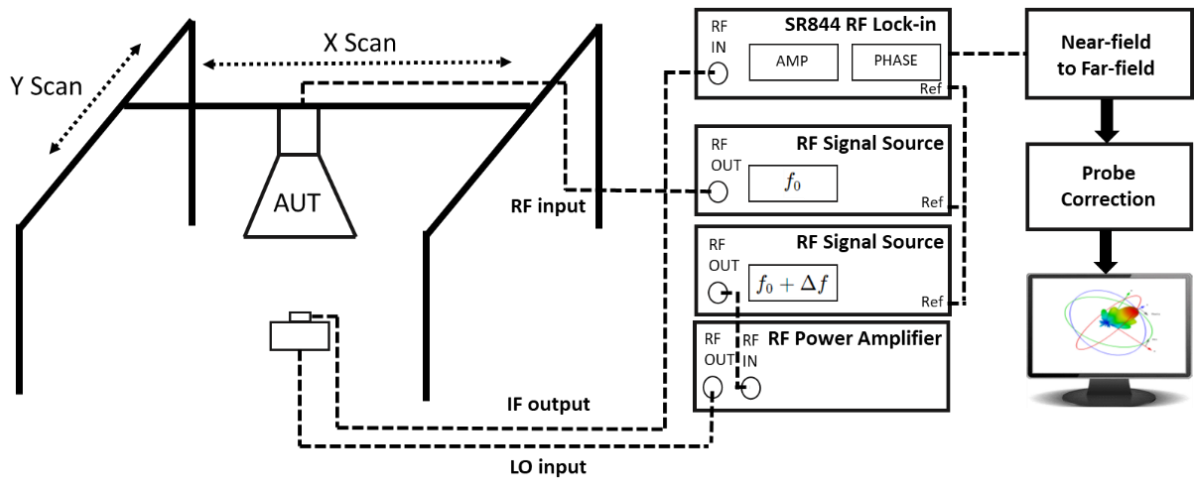

Figure 6.4 Complete view of the near-field measurement setup, and far-field calculation steps

6.4.1 Why use a Lock-In amplifier for detection?

Lock-In amplifiers are used to detect and measure very small signals. Lock-in amplifiers use a method known as Phase Sensitive Detection (PSD) to single out the component of the signal at a specific reference frequency and phase

[69]. It requires that the RF input to be an integer multiple of the reference signal which is 10 MHz in this case. As shown in Figure 6.5, the RF input gets multiplied by two orthogonal sinusoidal signals at the same frequency of RF input.

Using the outputs, amplitude and phase of the input signal can be detected:

$$R = \left(\frac{2}{V_R}\right) \times \sqrt{(V_{M1+Filter})^2 + (V_{M2+Filter})^2} \qquad (6.10)$$

$$\theta_R - \theta_I = tan^{-1}\left(\frac{V_{M1+Filter}}{V_{M2+Filter}}\right) \qquad (6.11)$$

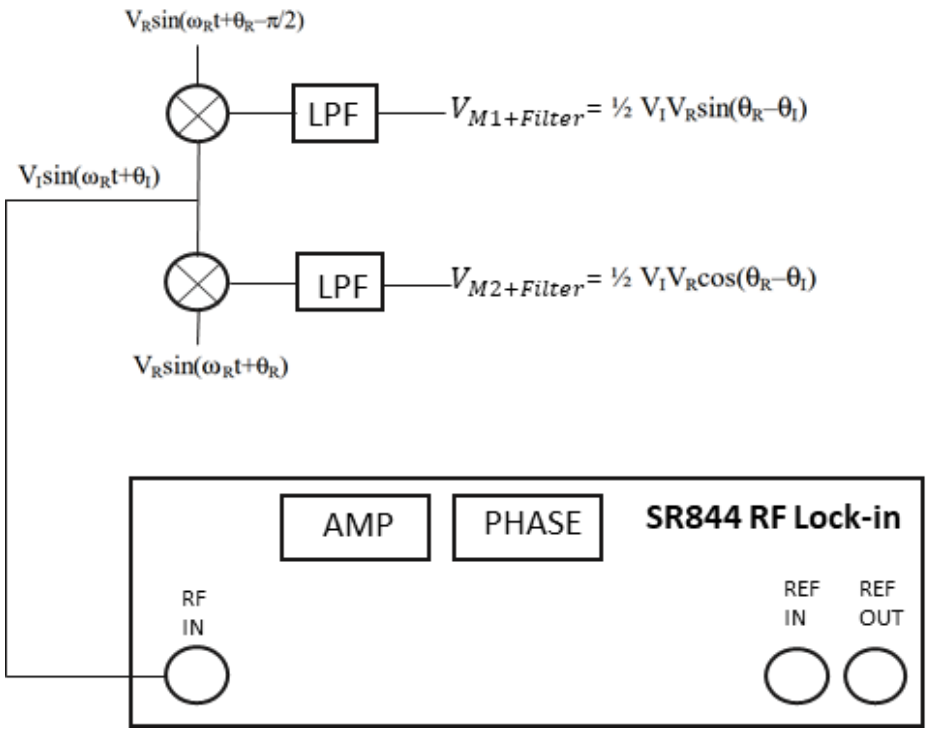

Figure 6. 5 Lock-in amplifier system diagram

In this system, noise signals at frequencies other than the reference frequency are rejected and do not affect the measurement. More accurate measurements can be made even when the dynamic range is improved. To do so,

an RF amplifier is used in this setup to work as a preamplifier to increase the LO power level, resulting in improving IF power, and enhancing signal-to-noise (SNR) ratio at the RF Lock-in Amplifier.

6.5 Probe Correction

Probe correction is essential in near-field measurements to compensate non-ideal probe's effect on calculated far-field based on the near-field. In the near-field measurements, the interaction of the near-field phase fronts between the AUT and probe antennas disturbs the true far-field pattern of an AUT. In probe correction, far-field radiation pattern of the probe is needed to be known. It can be measured directly or be accurately simulated in a 3D EM simulator.

The uncompensated far-field pattern of the AUT is product of the probe and AUT's true far-field patterns in spectral space due to the Fourier transform relations [67]. Therefore, in planar near-field measurements the non-ideal effect of the probe can be removed by measuring the AUT's near-field with two orthogonally polarized probes, transforming to the far-field and then adjusting each far-field value by the probe's directivity at that angle [67]. The AUT's true far-field pattern can be determined by dividing the uncompensated far-field pattern by the probe's far-field pattern if the probe's cross-polarization component is negligible. But if the cross-polarization component is significant,

as it would take part of the near-field cross-polarization, the effect of the cross-polarization needs to be considered. Therefore, there is such a relation between uncompensated far-field and compensated far-field:

$$E_{pu} = E_p \times E_{pp1} + E_c \times E_{cp1} \quad (6.12)$$

$$E_{cu} = E_p \times E_{cp2} + E_c \times E_{pp2} \quad (6.13)$$

where, E_p and E_c are true principal (or co-pol) and true cross-pol AUT response, respectively. E_{pu} and E_{cu} are uncompensated principal and cross-pol AUT response, respectively. And $E_{pp1/2}$ and $E_{cp1/2}$ are probe number 1/2 principal and cross-pol response, respectively. Equations (6.12), and (6.13) are written based on using two separate probes for co and cross polarization measurement; however, one probe can be used for both polarization while it is rotated for 90 degrees for the cross-polarization measurement [67]. In this case:

$$E_{pp2}(\emptyset) = E_{pp1}(\emptyset + 90) = E_{cp2}(\emptyset + 90) \quad (6.14)$$

Using equations (6.12) and (6.13), the true far-field can be calculated:

$$E_p = (E_{pp2} \times E_{pu} - E_{cp1} \times E_{cu})/\delta \quad (6.15)$$

$$E_c = (-E_{cp2} \times E_{pu} + E_{pp1} \times E_{cu})/\delta \quad (6.16)$$

$$\delta = E_{pp1} \times E_{pp2} - E_{cp1} \times E_{cp2}$$

If the cross polarization of the probe is negligible, (6.15) and (6.16) would become simplified to:

$$E_p = \frac{E_{pu}}{E_{pp1}} \quad (6.17)$$

$$E_c = \frac{E_{cu}}{E_{pp2}} \quad (6.18)$$

To accurately decompose the effect of the non-ideal probe from the far-field, the probe far-field pattern must avoid having any nulls in the angular region of space over which the test antenna pattern is determined [67]. Having nulls result in the probe correction coefficients to be infinite based on the equation pairs 6.15-6.16 or 6.17-6.18.

6.6 Far-field Calculation of an AUT's Measured Near-field

Based on discussions in the previous sections, and in the Chapter 5, the near-field is measured at distance of 10 cm, which is 3-4λ at the bandwidth of interest. The AUT is FXR X638A, an X-band standard gain horn antenna with 22 dBi gain. The probe is the one with the iris-coupled cavity waveguide which is discussed in Chapter 5. The setup is shown in Figure 6.6. The MATLAB programs prepared for this setup are documented in the Appendix I.

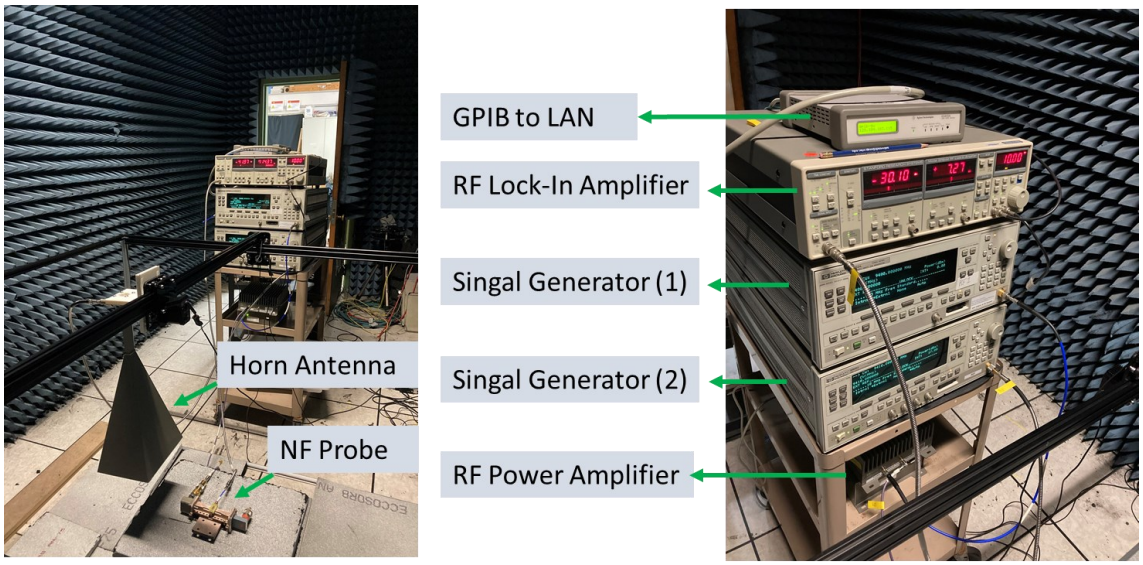

(a) (b)

Figure 6.6 Near-field measurement setup. (a) The probe setup and the near-field scanner, which is holding the horn antenna, and (b) the instruments rack consisting of two signal generators for RF and LO, an RF power amplifier for increasing power at LO port, an RF lock-in amplifier for the reception, and a GPIB to LAN gateway for transferring measured amplitude and phase from the RF lock-in amplifier to a computer.

Using the setup shown in Figure 6.6 near-field of the antenna under test (AUT) is measured at different frequencies for a 60 × 60 cm planar area at 10 cm far from the AUT. The near-field data is calibrated based on probe response simulated in CST Studio and partially depicted in Figure 5.11, and then transformed to far-field. But removing the effect of the probe pattern from the calculated far-field is required. In Figure 6.7, 6.8, 6.9, and 6.10, the calculated

and probe compensated far-field E-plane and H-plane of the AUT based on the measured near-field is compared to the uncompensated far-field and direct far-field of the AUT at 9 GHz, 9.5 GHz, 10 GHz, and 10.5 GHz, respectively.

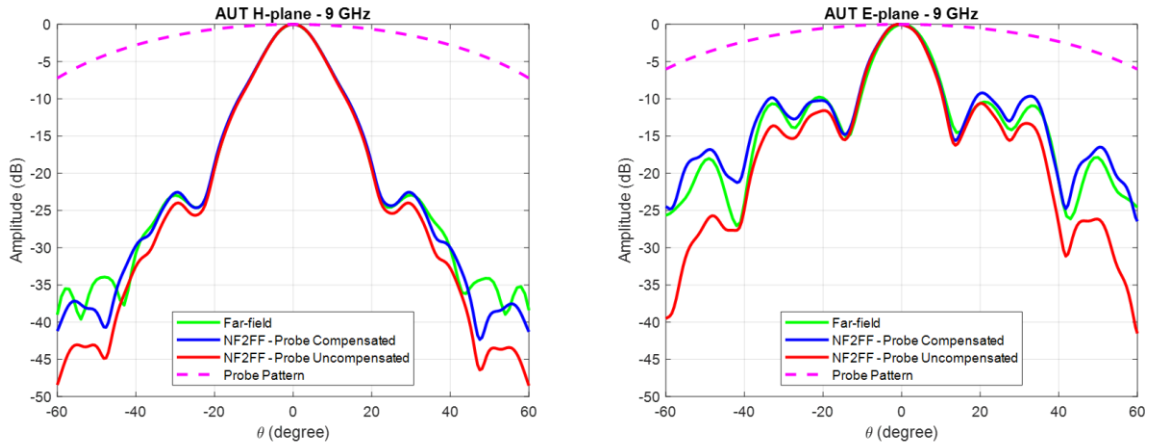

Figure 6.7 Comparison of probe compensated far-field with uncompensated and direct far-field at 9 GHz.

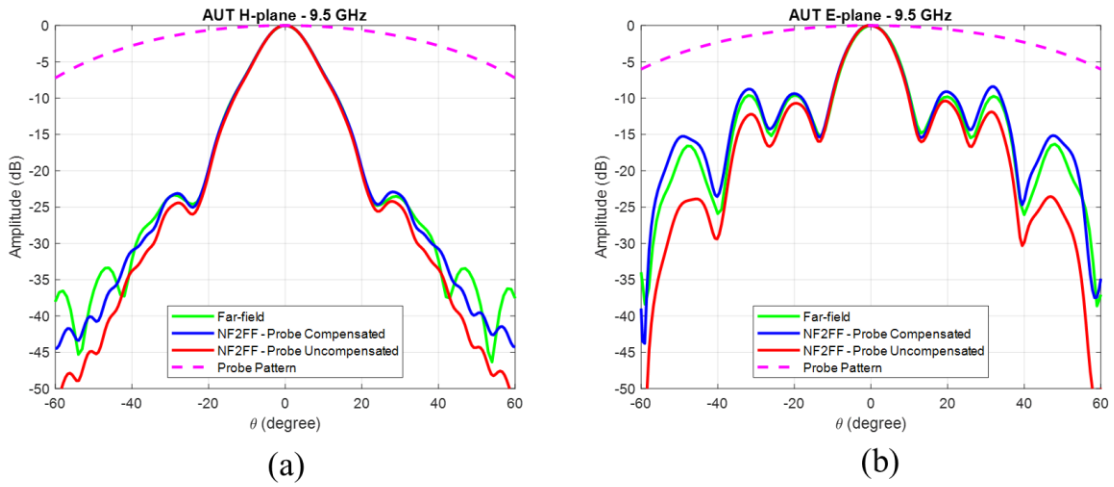

Figure 6.8 Comparison of probe compensated far-field with uncompensated and direct far-field at 9.5 GHz.

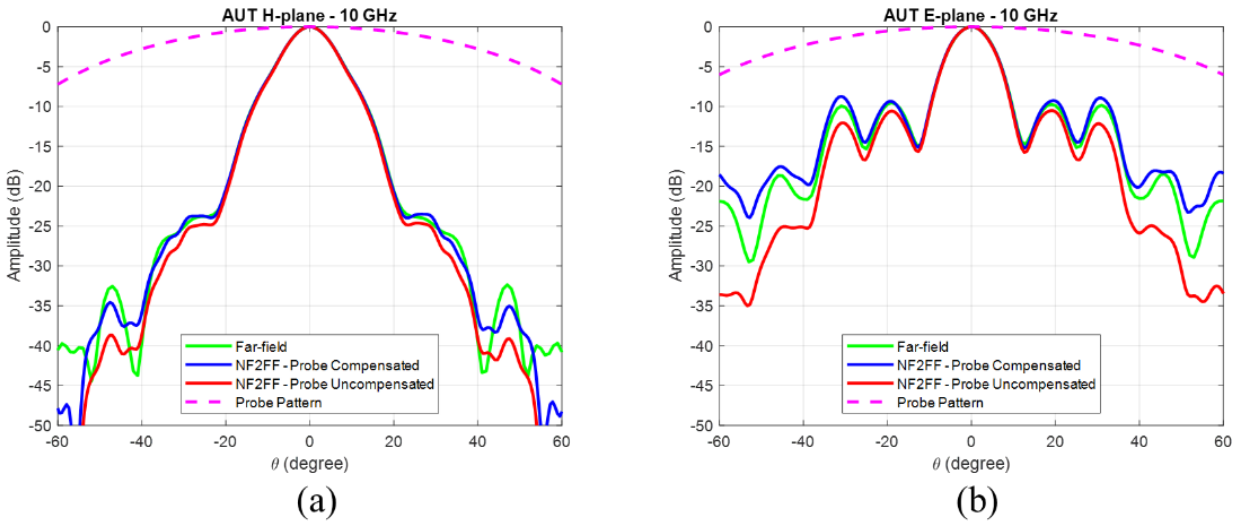

Figure 6.9 Comparison of probe compensated far-field with uncompensated and direct far-field at 10 GHz.

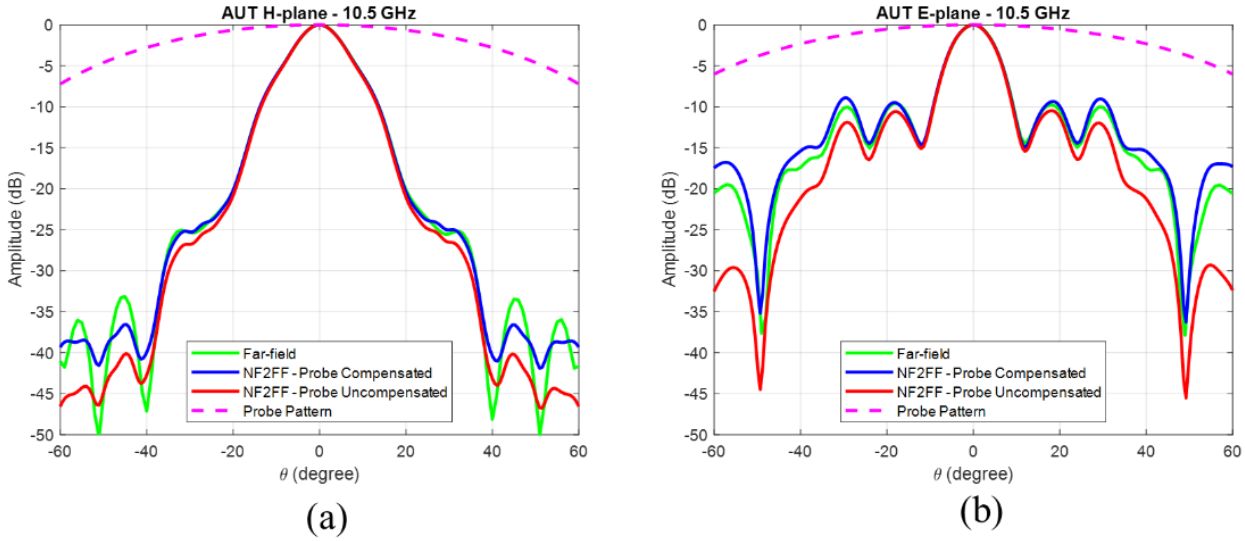

Figure 6.10 Comparison of probe compensated far-field with uncompensated and direct far-field at 10.5 GHz.

The results are based on the 60 × 60 cm near-field measurement at 10 cm distance to the AUT. They show the improvement of far-field result after probe

compensation. Also, they show that as frequency increases the compensated far-field, both E-plane and H-plane, have better agreement with the direct far-field. Using this setup, a low-cost planar near-field antenna measurement can be done. The proposed probe can be used in cylindrical or spherical near-field antenna measurement setups for other types of antennas.

7 CONCLUSION AND FUTURE WORK

In this thesis, fabrication of microwave components and antennas based on a 3-D printing and copper coating method discussed. New potentials discovered based on this method. Realization of microwave waveguide components using this method and then building a subsystem by cascading the components was the first proven capability by this method. A 3-D dipole antenna fed via a Marchand balun was an example of an antenna with fine internal features that was realized monolithically via this method. Also, two waveguide antennas designed based on unique features that 3-D printing gives us. With 3-D printing, the antenna designer can take the advantage of the third dimension to overcome some design challenges. The example for this was the slotted waveguide antenna that suffers from open stopband issue. By adding capacitive and inductive posts to the design as new features the issue was fixed. Lastly, an H-plane horn antenna with hard and soft walls was designed to benefit from 3D printing capabilities while improving directivity and front-to-back ratio.

In the Sections 5 and 6, I tried to tackle new challenges introduced by 5G to the antenna characterization. The idea was to avoid continuing using conventional measurement methods and lower the characterization cost while keeping the performance acceptable. For that, a novel probe was designed which

down-converts the RF signal to a low-frequency signal (IF signal) right at the probe plane via a mixer. Then, this probe was used in a planar near-field antenna measurement system. The results shows that the probe can cover the required dynamic range for the near-field measurement.

Major areas that the present work can be extended to:

(i) Design of a shorted dual-polarized proximity-fed patch antenna based on a waveguide feed.

(ii) Using new 3-D printing materials made for RF.

(iii) Using the proposed probe in a cylindrical setup.

(iv) Using a varactor diode to tune the slot probe to the desired frequency band.

8 REFERENCES

[1] Huang Guan-Long, Zhou Shi-Gang, Chio Tan-Huat and Yeo Tat-Soon, "3-D metal-direct-printed wideband and high-efficiency waveguide-fed antenna array," 2015 IEEE MTT-S International Microwave Symposium, 2015, pp. 1-4, doi: 10.1109/MWSYM.2015.7166882.

[2] C. Guo, X. Shang, M. J. Lancaster and J. Xu, "A 3-D Printed Lightweight X-Band Waveguide Filter Based on Spherical Resonators," in IEEE Microwave and Wireless Components Letters, vol. 25, no. 7, pp. 442-444, July 2015, doi: 10.1109/LMWC.2015.2427653.

[3] Design and Fabrication of 3D-Printed Planar Fresnel Zone Plate Lens. Electronics Letters

[4] blogs.3ds.com/simulia/5g-antenna-design-mobile-phones/.

[5] A. Georgiadis, J. Kimionis and M. M. Tentzeris, "3D/Inkjet-printed millimeter wave components and interconnects for communication and sensing," 2017 IEEE Compound Semiconductor Integrated Circuit Symposium (CSICS), 2017, pp. 1-4, doi: 10.1109/CSICS.2017.8240447.

[6] P. T. Timbie, J. Grade, D. van der Weide, B. Maffei and G. Pisano, "Stereolithographed MM-wave corrugated horn antennas," 2011 International Conference on Infrared, Millimeter, and Terahertz Waves, 2011, pp. 1-3, doi: 10.1109/irmmw-THz.2011.6104833.

[7] G. Venanzoni, M. Dionigi, C. Tomassoni and R. Sorrentino, "3-D-Printed Quasi-Elliptical Evanescent Mode Filter Using Mixed Electromagnetic Coupling," in IEEE Microwave and Wireless Components Letters, vol. 28, no. 6, pp. 497-499, June 2018, doi: 10.1109/LMWC.2018.2829627.

[8] E. A. Rojas-Nastrucci, J. T. Nussbaum, N. B. Crane and T. M. Weller, "Ka-Band Characterization of Binder Jetting for 3-D Printing of Metallic Rectangular Waveguide Circuits and Antennas," in IEEE Transactions on Microwave Theory and Techniques, vol. 65, no. 9, pp. 3099-3108, Sept. 2017, doi: 10.1109/TMTT.2017.2730839.

[9] H. Yao, L. Fang and R. Henderson, "Evaluating conductive paint performance on 3-D printed horn antennas," 2018 IEEE Radio and Wireless Symposium (RWS), 2018, pp. 191-193, doi: 10.1109/RWS.2018.8304983.

[10] A highly integrated 3-D printed metallick-band passive front end as the unit cell in a large array for satellite communication

[11] M. Dionigi, C. Tomassoni, G. Venanzoni and R. Sorrentino, "Simple High-Performance Metal-Plating Procedure for Stereolithographically 3-D-Printed Waveguide Components," in IEEE Microwave and Wireless Components Letters, vol. 27, no. 11, pp. 953-955, Nov. 2017, doi: 10.1109/LMWC.2017.2750090.

[12] A. Périgaud, S. Bila, O. Tantot, N. Delhote and S. Verdeyme, "3D printing of microwave passive components by different additive manufacturing technologies," 2016 IEEE MTT-S International Microwave Workshop Series on Advanced Materials and Processes for RF and THz Applications (IMWS-AMP), 2016, pp. 1-4, doi: 10.1109/IMWS-AMP.2016.7588328.

[13] formlabs.com/store/us/form-2/materials/durable-resin/.

[14] www.caswellplating.com/

[15] R. Cameron, R. Mansour, and C. Kudsia, Microwave filters for communication systems.

[16] Kim, Y.; Tentzeris, M.M.; Lim, S. Low-Loss and Light Substrate Integrated Waveguide Using 3D Printed Honeycomb Structure. Materials 2019, 12, 402. https://doi.org/10.3390/ma12030402

[17] M. D'Auria et al., "3-D Printed Metal-Pipe Rectangular Waveguides," in IEEE Transactions on Components, Packaging and Manufacturing Technology, vol. 5, no. 9, pp. 1339-1349, Sept. 2015, doi: 10.1109/TCPMT.2015.2462130.

[18] B. Zhang, R. Li, L. Wu, H. Sun and Y. Guo, "A Highly Integrated 3-D Printed Metallic K-Band Passive Front End as the Unit Cell in a Large Array for Satellite Communication," in IEEE Antennas and Wireless Propagation Letters, vol. 17, no. 11, pp. 2046-2050, Nov. 2018, doi: 10.1109/LAWP.2018.2824298.

[19] M. Kong, S. Lee, G. Shin, J. Nah and I. Yoon, "Investigation of 3-D Printed, Electrically Small, and Thin Magnetic Dipole Antenna," in IEEE Antennas and Wireless Propagation Letters, vol. 17, no. 4, pp. 654-657, April 2018, doi: 10.1109/LAWP.2018.2810238.

[20] P. Nayeri et al., "3D Printed Dielectric Reflectarrays: Low-Cost High-Gain Antennas at Sub-Millimeter Waves," in IEEE Transactions on Antennas and Propagation, vol. 62, no. 4, pp. 2000-2008, April 2014, doi: 10.1109/TAP.2014.2303195.

[21] O. A. Peverini et al., "Selective Laser Melting Manufacturing of Microwave Waveguide Devices," in Proceedings of the IEEE, vol. 105, no. 4, pp. 620-631, April 2017, doi: 10.1109/JPROC.2016.2620148.

[22] M. Liang, C. Shemelya, E. MacDonald, R. Wicker and H. Xin, "3-D Printed Microwave Patch Antenna via Fused Deposition Method and Ultrasonic Wire Mesh Embedding Technique," in IEEE Antennas and Wireless Propagation Letters, vol. 14, pp. 1346-1349, 2015, doi: 10.1109/LAWP.2015.2405054.

[23] E. G. Geterud, P. Bergmark and J. Yang, "Lightweight waveguide and antenna components using plating on plastics," 2013 7th European Conference on Antennas and Propagation (EuCAP), 2013, pp. 1812-1815.

[24] Bal, A, Carey, DG, Espinal, FA & Huff, GH 2019, 'Electroless silver plating of 3D printed waveguide components by peristaltic pump driven system', Electronics Letters, vol. 55, no. 2, pp. 100-102. https://doi.org/10.1049/el.2018.7288

[25] Castro, Alejandro T.; Babakhani, Behrouz; Sharma, Satish K.: 'Design and development of a multimode waveguide corrugated horn antenna using 3D printing technology and its comparison with aluminium-based prototype', IET Microwaves, Antennas & Propagation, 2017, 11, (14), p. 1977-1984, DOI: 10.1049/iet-map.2016.0808

[26] H. Saeidi-Manesh, S. Saeedi, M. Mirmozafari, G. Zhang and H. H. Sigmarsson, "Design and Fabrication of Orthogonal-Mode Transducer Using 3-D Printing Technology," in IEEE Antennas and Wireless Propagation Letters, vol. 17, no. 11, pp. 2013-2016, Nov. 2018, doi: 10.1109/LAWP.2018.2847654.

[27] M. Ranjbar Naeini and D. van der Weide, "Cascaded 3-D-Printed X-Band Components for Subsystems," in IEEE Microwave and Wireless Components Letters, vol. 29, no. 5, pp. 333-335, May 2019, doi: 10.1109/LMWC.2019.2905986.

[28] M. Mirmozafari, S. Saeedi, H. Saeidi-Manesh, G. Zhang and H. H. Sigmarsson, "Direct 3-D Printing of Nonplanar Linear-Dipole-Phased Array Antennas," in IEEE Antennas and Wireless Propagation Letters, vol. 17, no. 11, pp. 2137-2140, Nov. 2018, doi: 10.1109/LAWP.2018.2860463.

[29] Roberts, Willmar K.. "A New Wide-Band Balun." Proceedings of the IRE 45 (1957): 1628-1631.

[30] Yao, Haohan et al. "Ka band 3D printed horn antennas." 2017 Texas Symposium on Wireless and Microwave Circuits and Systems (WMCS) (2017): 1-4.

[31] Y. Álvarez et al., "Submillimeter-Wave Frequency Scanning System for Imaging Applications," in IEEE Transactions on Antennas and Propagation, vol. 61, no. 11, pp. 5689-5696, Nov. 2013, doi: 10.1109/TAP.2013.2275747.

[32] K. van Caekenberghe, K. F. Brakora and K. Sarabandi, "A 94 GHz OFDM Frequency Scanning Radar for Autonomous Landing Guidance," 2007 IEEE Radar Conference, 2007, pp. 248-253, doi: 10.1109/RADAR.2007.374222.

[33] Saeidi-Manesh, H.; Mirmozafari, M.; Zhang, G.: 'Low cross-polarisation high-isolation frequency scanning aperture coupled microstrip patch antenna array with matched dual-polarisation radiation patterns', Electronics Letters, 2017, 53, (14), p. 901-902, DOI: 10.1049/el.2017.1282

[34] Tehrani, Mona Akbarniai et al. “Multiple targets direction-of-arrival estimation in frequency scanning array antennas.” Iet Radar Sonar and Navigation 10 (2016): 624-631.

[35] S. Karimkashi et al., "Dual-Polarization Frequency Scanning Microstrip Array Antenna With Low Cross-Polarization for Weather Measurements," in IEEE Transactions on Antennas and Propagation, vol. 61, no. 11, pp. 5444-5452, Nov. 2013, doi: 10.1109/TAP.2013.2279996.

[36] S. Shad and H. Mehrpouyan, "A Dielectric-Loaded Waveguide Aperture Antenna Based on Waveguide-Fed Cavity-Backed in the 60-GHz Band," 2019 IEEE Texas Symposium on Wireless and Microwave Circuits and Systems (WMCS), 2019, pp. 1-4, doi: 10.1109/WMCaS.2019.8732492.

[37] Jackson, D. et al. “Leaky-Wave Antennas.” Proceedings of the IEEE 100 (2012): 2194-2206.

[38] S. Xu et al., "A Wide-Angle Narrowband Leaky-Wave Antenna Based on Substrate Integrated Waveguide-Spoof Surface Plasmon Polariton Structure," in IEEE Antennas and Wireless Propagation Letters, vol. 18, no. 7, pp. 1386-1389, July 2019, doi: 10.1109/LAWP.2019.2917561.

[39] Ranjbar Naeini, M., Fakharzadeh, M. & Farzaneh, F. Ka-band Frequency Scanning Antenna with Wide-Angle Span. J Infrared Milli Terahz Waves 40, 231–246 (2019).

[40] A. Mallahzadeh and S. Mohammad-Ali-Nezhad, "Periodic Collinear-Slotted Leaky Wave Antenna With Open Stopband Elimination," in IEEE Transactions on Antennas and Propagation, vol. 63, no. 12, pp. 5512-5521, Dec. 2015, doi: 10.1109/TAP.2015.2484424.

[41] M. D’Auria et al., "3-D Printed Metal-Pipe Rectangular Waveguides," in IEEE Transactions on Components, Packaging and Manufacturing Technology, vol. 5, no. 9, pp. 1339-1349, Sept. 2015, doi: 10.1109/TCPMT.2015.2462130.

[42] G. P. Le Sage, "3D Printed Waveguide Slot Array Antennas," in IEEE Access, vol. 4, pp. 1258-1265, 2016, doi: 10.1109/ACCESS.2016.2544278.

[43] M. Dionigi, C. Tomassoni, G. Venanzoni and R. Sorrentino, "Simple High-Performance Metal-Plating Procedure for Stereolithographically 3-D-Printed Waveguide Components," in IEEE Microwave and Wireless Components Letters, vol. 27, no. 11, pp. 953-955, Nov. 2017, doi: 10.1109/LMWC.2017.2750090.

[44] E. Arnieri, L. Boccia, G. Amendola and G. Di Massa, "A Compact High Gain Antenna for Small Satellite Applications," in IEEE Transactions on Antennas and Propagation, vol. 55, no. 2, pp. 277-282, Feb. 2007, doi: 10.1109/TAP.2006.889831.

[45] R. E. Hodges, N. Chahat, D. J. Hoppe and J. D. Vacchione, "A Deployable High-Gain Antenna Bound for Mars: Developing a new folded-panel reflectarray for the first CubeSat mission to Mars.," in IEEE Antennas and Propagation Magazine, vol. 59, no. 2, pp. 39-49, April 2017, doi: 10.1109/MAP.2017.2655561.

[46] Zhang, Jieqiu et al. “Dual-band bidirectional high gain antenna for WLAN 2.4/5.8 GHz applications.” Electronics Letters 45 (2009): 6-7.

[47] Tolkachev, A. et al. “High gain antenna systems for millimeter wave radars with combined electronical and mechanical beam steering.” Proceedings of International Symposium on Phased Array Systems and Technology (1996): 266-271.

[48] S. Shad and H. Mehrpouyan, "60 GHz Waveguide-Fed Cavity Array Antenna by Multistepped Slot Aperture," in IEEE Antennas and Wireless Propagation Letters, vol. 19, no. 3, pp. 438-442, March 2020, doi: 10.1109/LAWP.2020.2966149.

[49] D. Sanchez-Escuderos, M. Ferrando-Bataller, A. Berenguer and M. Baquero-Escudero, "Design of an H-plane horn array antenna using the complete 1D/3D-EBG waveguide in the THz band," 2012 6th European Conference on Antennas and Propagation (EUCAP), 2012, pp. 2343-2347, doi: 10.1109/EuCAP.2012.6206078.

[50] N. Bayat-Makou and A. A. Kishk, "Substrate Integrated Horn Antenna With Uniform Aperture Distribution," in IEEE Transactions on Antennas and Propagation, vol. 65, no. 2, pp. 514-520, Feb. 2017, doi: 10.1109/TAP.2016.2640144.

[51] Y. Zhao, Z. Shen and W. Wu, "Wideband and Low-Profile H-Plane Ridged SIW Horn Antenna Mounted on a Large Conducting Plane," in IEEE Transactions on Antennas and Propagation, vol. 62, no. 11, pp. 5895-5900, Nov. 2014, doi: 10.1109/TAP.2014.2354420.

[52] K. Iigusa, K. Li, K. Sato and H. Harada, "Gain Enhancement of H-Plane Sectoral Post-Wall Horn Antenna by Connecting Tapered Slots for Millimeter-Wave Communication," in IEEE Transactions on Antennas and Propagation, vol. 60, no. 12, pp. 5548-5556, Dec. 2012, doi: 10.1109/TAP.2012.2214193.

[53] H. Wang, D. Fang, B. Zhang and W. Che, "Dielectric Loaded Substrate Integrated Waveguide (SIW) H-Plane Horn Antennas," in IEEE Transactions on Antennas and Propagation, vol. 58, no. 3, pp. 640-647, March 2010, doi: 10.1109/TAP.2009.2039298.

[54] A. R. Mallahzadeh and S. Esfandiarpour, "Wideband H-Plane Horn Antenna Based on Ridge Substrate Integrated Waveguide (RSIW)," in IEEE Antennas and Wireless Propagation Letters, vol. 11, pp. 85-88, 2012, doi: 10.1109/LAWP.2012.2183110.

[55] M. Ranjbar Naeini, M. Mirmozafari and D. van der Weide, "Monolithic 3-D Printing of an Integrated Marchand Balun With a Dipole Antenna," in IEEE Transactions on Components, Packaging and Manufacturing Technology, vol. 10, no. 4, pp. 654-658, April 2020, doi: 10.1109/TCPMT.2020.2966535.

[56] D. Miek, S. Simmich, F. Kamrath and M. Höft, "Additive Manufacturing of E-Plane Cut Dual-Mode X-Band Waveguide Filters With Mixed Topologies," in IEEE Transactions on Microwave Theory and Techniques, vol. 68, no. 6, pp. 2097-2107, June 2020, doi: 10.1109/TMTT.2020.2981057.

[57] Aşcı, Yavuz & Yegin, Korkut. (2019). Additively manufactured trapezoidal grooves for wideband and high gain Ku-band antenna. International Journal of RF and Microwave Computer-Aided Engineering. 30. 10.1002/mmce.22089.

[58] C. A. Balanis, Antenna Theory: Analysis and Design, 3rd ed. Hoboken.

[59] E. Lier and P. -. Kildal, "Soft and hard horn antennas," in IEEE Transactions on Antennas and Propagation, vol. 36, no. 8, pp. 1152-1157, Aug. 1988, doi: 10.1109/8.7229.

[60] P. Kildal, "Artificially soft and hard surfaces in electromagnetics," in IEEE Transactions on Antennas and Propagation, vol. 38, no. 10, pp. 1537-1544, Oct. 1990, doi: 10.1109/8.59765.

[61] M. Jokinen, O. Kursu, N. Tervo, J. Saloranta, M. E. Leinonen and A. Pärssinen, "Over-the-Air Phase Measurement and Calibration Method for 5G mmW Phased Array Radio Transceiver," 2019 93rd ARFTG Microwave Measurement Conference (ARFTG), 2019, pp. 1-4, doi: 10.1109/ARFTG.2019.8739190.

[62] J. Moon and J. Yun, "The Design of Broadband Probe for Efficient Near Field Measurements," in IEEE Antennas and Wireless Propagation Letters, vol. 6, pp. 440-443, 2007, doi: 10.1109/LAWP.2007.904713.

[63] W. Liang, G. Hygate, J. F. Nye, D. G. Gentle and R. J. Cook, "A probe for making near-field measurements with minimal disturbance: the optically modulated scatterer," in IEEE Transactions on Antennas and Propagation, vol. 45, no. 5, pp. 772-780, May 1997, doi: 10.1109/8.575620.

[64] S. Kittiwittayapong, K. Phaebua, P. Sittithai and T. Lertwiriyaprapa, "Low-cost planar near-field to far-field measurement system for a small antenna," 2016 13th International Conference on Electrical Engineering/Electronics, Computer, Telecommunications and Information Technology (ECTI-CON), 2016, pp. 1-3, doi: 10.1109/ECTICon.2016.7561464.

[65] M. Alonso-delPino, M. d. Rosa, M. Simeoni, M. Spella, C. De Martino and M. Spirito, "A Planar Near-Field Setup for Millimeter-Wave System-Embedded Antenna Testing," in IEEE Antennas and Wireless Propagation Letters, vol. 16, pp. 83-86, 2017, doi: 10.1109/LAWP.2016.2557239.

[66] “Keysight Technologies OTA Test for Millimeter-Wave 5G NR Devices and Systems,” [Online]. Available: https://www.keysight.com/us/en/assets/7018-05940/white-papers/5992-2600.pdf.

[67] D. Paris, W. Leach and E. Joy, "Basic theory of probe-compensated near-field measurements," in IEEE Transactions on Antennas and Propagation, vol. 26, no. 3, pp. 373-379, May 1978, doi: 10.1109/TAP.1978.1141855.

[68] K. Van Caekenberghe, J. Logan, “NF2FF”, MATLAB Central File Exchange. Retrieved June 15, 2021. https://www.mathworks.com/matlabcentral/fileexchange/23385-nf2ff,

[69] S. R. Systems, “Model SR844 RF Lock-In Amplifier”.

APPENDIX I

In this appendix, MATLAB programs prepared for the measurement of the near-field system are put for further applications.

1- Connecting to the near-field scanner and the RF Lock-in amplifier.

%Connect to Scanner and RF Lock-in

```
clc
clear
close all

if ~isempty(instrfind)
    fclose(instrfind);
     delete(instrfind);
end

%% Start creating serial object, initialize the driver box
s = serial('COM10');
fopen(s);
set(s,'BaudRate',115200);
out = fscanf(s)
out = fscanf(s)

%% RF Lock In Setup

LIN=visa('keysight', 'GPIB1::8::INSTR')
% LIN = gpib('keysight', 11, 8);% alternative
fopen(LIN);
Amp_dbm=str2num(query(LIN, 'OUTR?1'))
Phase_deg=str2num(query(LIN, 'OUTR?2'))
```

```
fclose(LIN);
```

For data acquisition from the RF Lock-in amplifier a GPIB to LAN gateway is used. Keysight has prepared a software called Keysight Connection Expert which helps setting up this device.

2- Scan and Data Acquisition

After initialization of the setup, we should run the MATLAB program for scanning and data acquisition.

```
clc

test_datetime=fix(clock);
% the test name includes the date and time of the test
testname=['Test',num2str(test_datetime(1)),'_',num2str(test_datetime(2)),'_',num2str(test_datetime(3))
,'_',num2str(test_datetime(4)),'_',num2str(test_datetime(5)),'_',num2str(test_datetime(6))]

%% Task specific parameters(all in mm)
% it is recommended to write notes about the setup, the notes will be saved
% with the data for further reference.
Notes="Freq=10 GHz, Distance=10cm, Cavity filter waveguide after 3rd coat , COpol";
stepSize = 50;
scan_width=800; % Width of the Scan
scan_height=800; % Height of the Scan

scan_width=scan_width*2;
scan_height=scan_height*2;

totalX = ceil(scan_width/stepSize);
totalY = ceil(scan_height/stepSize);

xp = 0;
```

```
yp = 0;

fopen(LIN);

final_data(totalY/2,totalX/2)=0;   %

   first_pass=0;
for yp=1:totalY/2
   if yp==1
      tic
   end
   progress=yp/totalY*2;
   if yp~=1
   close(h)
   end
   h=waitbar(progress,['Scanning Progress  %',num2str(progress*100),' Time Left : ',num2str(round((1-
progress)*totalY/2*first_pass/60,2,'significant')),'min'])
   for xp = 1:totalX/2
      Amp=10^((str2num(query(LIN, 'OUTR?1'))-30)/10);
      Phase_deg=str2num(query(LIN, 'OUTR?2'));
      final_data(xp,yp) = Amp*exp(1i*pi*Phase_deg/180);
      MoveYDown(s,num2str(stepSize));
      fprintf(s,'G4P0');
      xdataRdy(s);
      pause(1)
   end

   if (xp == totalX/2) && (yp == totalY/2)
      break;  %the end of scanning area
   else
      MoveYUp(s,num2str(scan_width/2));
      fprintf(s,'G4P0');
      xdataRdy(s);
      pause(1)

      MoveXLeft(s,num2str(stepSize)); % to move Y down for 1 step
```

```
        fprintf(s,'G4P0');
        ydataRdy(s);
        pause(1)
    end
    if yp==1
        first_pass=toc
    end
    disp(['Estimated Time : ', num2str(totalY*first_pass),'sec'])
end
MoveXRight(s,num2str(ceil(scan_width/2)-stepSize));
fprintf(s,'G4P0');
        xdataRdy(s);
        pause(1)
MoveYUp(s,num2str(ceil(scan_height/2)));
fprintf(s,'G4P0');
        xdataRdy(s);
        pause(1)

save([num2str(testname),'.mat'],'final_data','Notes')
email_test([num2str(testname),'.mat'],'ranjbarnaein@wisc.edu');%send an email when the test is done with the data attached to the email address
% the data is sent to the given email address.
'Done!'
fclose(LIN);
figure
surf(db(abs(final_data))/2-max(max(db(abs(final_data))/2))); % the raw near-field data is plotted
colormap('jet')
```

3- Near-field to far-field calculation

Then the near-field to far-field calculation is done based on the published MATLAB program at [67]. The program with some few modifications is:

% Near-Field to Far-Field Transformation for Antenna Measurements (NF2FF)

% The script assumes:

% 1. Rectangular coordinate system with z axis normal to planar aperture

% The reference is : Van Caekenberghe, K.; Logan, J. (2021). NF2FF (https://www.mathworks.com/matlabcentral/fileexchange/23385-nf2ff), MATLAB Central File Exchange. Retrieved June 15, 2021.

```
clc;
close all;
clear all;

freq=10e9;
c=3e8; % Speed of light in vacuum [m/s]
load('horn_near_field_measured_z_30cm.mat')%

mm=0;
nn=0;
z_meas=0.1;%meter
xbound=0.3;
ybound=0.3;
step=0.015;
xx=-xbound:step:xbound;
yy=-ybound:step:ybound;
data_co(length(xx),length(yy))=0;
data_cross(length(xx),length(yy))=0;
z_dis=0.31;%meter

for m1=xx
   mm=mm+1;
   [E, H] = EHfields(horn_antennaDesigner, freq, [m1*ones(1,length(yy));yy;ones(1,length(yy))*z_dis]);
```

```
    data_co(mm,:)=E(1,:);
    data_cross(mm,:)=E(2,:);

end

%% Initial Setup
prob_comp=1;
Eplane_cut=90;
freq_des=freq;%freq  (GHz)
x_step=step*1000;%mm
y_step=step*1000;%mm
z0=z_meas;%distance to AUT (m)
Compare_with_Sim=0; %Compare with Sim Yes=1 No=0
%%
s21=data_co;
s21_cross=data_cross;

[M N]=size(s21);
dx=x_step/1000; % Sample spacing in the x direction [m]
dy=y_step/1000; % Sample spacing in the y direction [m]

% See equations (16-10a) and (16-10b) in Balanis
a=dx*(M-1); % The length of the scanned area in the x direction [m]
b=dy*(N-1); % The length of the scanned area in the y direction [m]
x=[-a/2:a/(M-1):a/2];
y=[-b/2:b/(N-1):b/2];

% See equations (16-13a) and (16-13b) in Balanis
% Zero padding is used to increase the resolution of the plane wave spectral domain.
% MI=4*M;%2^(ceil(log2(M))+1);
% NI=4*N;%2^(ceil(log2(N))+1);
MI=4*M;
NI=4*N;
m=[-MI/2:1:MI/2-1];
n=[-NI/2:1:NI/2-1];
k_X_Rectangular=2*pi*m/(MI*dx);
```

```
k_Y_Rectangular=2*pi*n/(NI*dy);
[k_Y_Rectangular_Grid,k_X_Rectangular_Grid] = meshgrid(k_Y_Rectangular,k_X_Rectangular);

dtheta=0.01;
dphi=0.01;
theta=[-pi/2+dtheta:dtheta:pi/2-dtheta];

phi=[0+dphi:dphi:pi-dphi];
[theta,phi]=meshgrid(theta,phi);

f=freq;
lambda0=c/f;
k0=2*pi/lambda0;
k_Z_Rectangular_Grid = sqrt(k0^2-k_X_Rectangular_Grid.^2-k_Y_Rectangular_Grid.^2);


for iy=1:1:N
   for ix=1:1:M
      NF_X_Complex(ix,iy)=s21(ix,iy);
      NF_Y_Complex(ix,iy)=s21_cross(ix,iy);
   end
end



NF_X_Magnitude = db(abs(NF_X_Complex));
NF_Y_Magnitude = db(abs(NF_Y_Complex));

figure;
subplot(2,1,1)
surf(x*1000,y*1000,NF_X_Magnitude');
title(sprintf('f = %f GHz (z = %i mm)',f/1000000000,z0*1000));
xlabel('x (mm)');
ylabel('y (mm)');
zlabel('|E_{x}| (dB)');
set(gca,'XLim',[min(x)*1000 max(x)*1000]);
```

```
set(gca,'YLim',[min(y)*1000 max(y)*1000]);
view(-37.5,30);
shading flat;
colorbar;
subplot(2,1,2);
surf(x*1000,y*1000,NF_Y_Magnitude');
xlabel('x (mm)');
ylabel('y (mm)');
zlabel('|E_{y}| (dB)');
set(gca,'XLim',[min(x)*1000 max(x)*1000]);
set(gca,'YLim',[min(y)*1000 max(y)*1000]);
view(-37.5,30);
shading flat;
colorbar;
clear NF_X_Magnitude NF_Y_Magnitude;


f_X_Rectangular=ifftshift(ifft2(NF_X_Complex,MI,NI));
f_Y_Rectangular=ifftshift(ifft2(NF_Y_Complex,MI,NI));
f_Z_Rectangular=-
(f_X_Rectangular.*k_X_Rectangular_Grid+f_Y_Rectangular.*k_Y_Rectangular_Grid)./k_Z_Rectan
gular_Grid;


f_X_Rectangular_Magnitude=20*log10(abs(f_X_Rectangular));
f_Y_Rectangular_Magnitude=20*log10(abs(f_Y_Rectangular));
f_Z_Rectangular_Magnitude=20*log10(abs(f_Z_Rectangular));



% Holographic back projection
for iy = 1:1:NI
   for ix = 1:1:MI
      if(isreal(k_Z_Rectangular_Grid(ix,iy))) % propagating or evanescent?
         f_X_z0_Rectangular(ix,iy)=f_X_Rectangular(ix,iy)*exp(j*k_Z_Rectangular_Grid(ix,iy)*z0);
         f_Y_z0_Rectangular(ix,iy)=f_Y_Rectangular(ix,iy)*exp(j*k_Z_Rectangular_Grid(ix,iy)*z0);
         f_Z_z0_Rectangular(ix,iy)=-
(f_X_z0_Rectangular(ix,iy)*k_X_Rectangular_Grid(ix,iy)+f_Y_z0_Rectangular(ix,iy)*k_Y_Rectang
ular_Grid(ix,iy))/k_Z_Rectangular_Grid(ix,iy);
      else
```

```
            f_X_z0_Rectangular(ix,iy)=0;
            f_Y_z0_Rectangular(ix,iy)=0;
            f_Z_z0_Rectangular(ix,iy)=0;
        end
    end
end

f_X_Spherical=interp2(k_X_Rectangular,k_Y_Rectangular,abs(f_X_Rectangular'),k0*sin(theta).*cos(phi),k0*sin(theta).*sin(phi),'spline');
f_Y_Spherical=interp2(k_X_Rectangular,k_Y_Rectangular,abs(f_Y_Rectangular'),k0*sin(theta).*cos(phi),k0*sin(theta).*sin(phi),'spline');
f_Z_Spherical=interp2(k_X_Rectangular,k_Y_Rectangular,abs(f_Z_Rectangular'),k0*sin(theta).*cos(phi),k0*sin(theta).*sin(phi),'spline');

r=10000;
C=j*(k0*exp(-j*k0*r))/(2*pi*r);
Etheta=C*(f_X_Spherical.*cos(phi)+f_Y_Spherical.*sin(phi));
Ephi=C*cos(theta).*(-f_X_Spherical.*sin(phi)+f_Y_Spherical.*cos(phi));


W=1/(2*120*pi).*(Etheta.*conj(Etheta)+Ephi.*conj(Ephi));

U = (abs(Etheta).^2 + abs(Ephi).^2);

% Calculation of radiated power through numerical integration
e_theta = [1 4 repmat([2 4], 1, floor(length(theta(1,:))/2) - 1) 1];
e_phi = [1 4 repmat([2 4], 1, floor(length(phi(:,1))/2) - 1) 1];
P = dphi*dtheta*sum(sum(U.*(e_theta'*e_phi).*abs(sin(theta))))/9;

W_Size=size(W);
EPLANE(1,:)=10*log10(W(floor(W_Size(2)/2),:))-max(10*log10(W(floor(W_Size(2)/2),:)));
HPLANE(1,:)=10*log10(W(1,:).*cos(theta(1,:)).^(-1))-max(10*log10(W(1,:)));

figure
vv=patternElevation(horn_antennaDesigner,freq,90);
vv=[vv(91:end);vv(1:90)]
plot(-180:1:180,vv)
```

```
hold on
plot(180/pi*theta(1,:),EPLANE+21.92,'r');
% plot(180/pi*theta(1,:),EPLANE_C+21.92,'r');

% if Compare_with_Sim==1
% plot(E_pattern_sim_theta,E_pattern_sim_mag-max(E_pattern_sim_mag),'b')
% end
title(['E-Plane at ',num2str(freq),'GHz']);
xlabel('\theta (Deg)');
ylabel('Directivity (dBi)');
set(gca,'XLim',[-90 90]);

movegui('west');



figure
hh=patternElevation(horn_antennaDesigner,freq,0);
hh=[hh(91:end);hh(1:90)]
plot(-180:1:180,hh)
hold on
plot(180/pi*theta(1,:),HPLANE-max(HPLANE)+24,'r');
title('H-Plane');
xlabel('\theta (Deg)');
ylabel('Directivity (dBi)');
set(gca,'XLim',[-90 90]);
set(gca,'YLim',[-25 23]);
movegui('east');
```